Journal of Applied Physics

RESEARCH ARTICLE | JUNE 16 2023

Self-consistent simulations of intracavity terahertz comb difference frequency generation by mid-infrared quantum cascade lasers

Johannes Popp ; Lukas Seitner ; Michael A. Schreiber ; Michael Haider ; Luigi Consolino ; Alessia Sorgi; Francesco Cappelli ; Paolo De Natale ; Kazuue Fujita ; Christian Jirauschek

J. Appl. Phys. 133, 233103 (2023)
https://doi.org/10.1063/5.0151036

Journal of Applied Physics ARTICLE scitation.org/journal/jap

Self-consistent simulations of intracavity terahertz comb difference frequency generation by mid-infrared quantum cascade lasers

Cite as: J. Appl. Phys. **133**, 233103 (2023); doi: 10.1063/5.0151036
Submitted: 17 March 2023 · Accepted: 26 May 2023 ·
Published Online: 16 June 2023

Johannes Popp,[1,a)] Lukas Seitner,[1] Michael A. Schreiber,[1] Michael Haider,[1] Luigi Consolino,[2,3] Alessia Sorgi,[2,3] Francesco Cappelli,[2,3] Paolo De Natale,[2,3] Kazuue Fujita,[4] and Christian Jirauschek[1,5]

AFFILIATIONS

[1]TUM School of Computation, Information and Technology, Technical University of Munich (TUM), D-85748 Garching, Germany
[2]CNR-Istituto Nazionale di Ottica, Largo Enrico Fermi 6, 50125 Firenze, Italy
[3]European Laboratory for Non-linear Spectroscopy, Via N. Carrara 1, 50019 Sesto Fiorentino, Italy
[4]Central Research Laboratory, Hamamatsu Photonics K.K., 5000 Hirakuchi, Hamakita-ku, Hamamatsu 434-8601, Japan
[5]TUM Center for Quantum Engineering (ZQE), Technical University of Munich (TUM), D-85748 Garching, Germany

[a)]**Author to whom correspondence should be addressed:** johannes.popp@tum.de

ABSTRACT

Portable terahertz (THz) frequency comb sources are highly desired for applications in rotational molecular spectroscopy and sensing. To date, direct THz quantum cascade laser (QCL) frequency comb generation is not achievable at room temperature. However, THz comb generation based on intracavity difference frequency generation (DFG) in mid-infrared (mid-IR) QCLs is a promising alternative. Here, we present a numerical study of THz DFG-QCL comb formation in mid-IR QCLs based on a self-consistent multi-domain simulation approach. The dynamical simulations are performed using our open-source software tool mbsolve, which provides a flexible and efficient codebase for solving the generalized full-wave Maxwell–Bloch equations. Here, DFG in the active region of a dual-wavelength mid-IR QCL is considered for the generation of THz radiation. The mixing process and, thus, THz generation require a high second-order intersubband nonlinear susceptibility in the QCL active region and can be obtained by targeted quantum engineering. The associated nonlinear effects are included in the Hamiltonian of our Maxwell–Bloch simulation approach. All necessary input parameters for the description of the quantum system are determined self-consistently using our in-house ensemble Monte Carlo software tool for stationary carrier transport simulations. Notably, such simulations require a full-wave Maxwell–Bloch solver that does not employ the common rotating wave approximation, as a broadband optical field extending from the THz to the mid-IR region is investigated. Our modeling approach and the obtained simulation results for two THz DFG-QCL comb setups are validated against experimental data, showing reasonable agreement. Furthermore, we obtain a locked frequency modulated comb state for mid-IR and THz regimes.

I. INTRODUCTION

The quantum cascade laser is a peculiar type of semiconductor laser, where the emission frequency is selected by quantum engineering. Here, the optical transition takes place between quantized electron states in the conduction band of a multiple quantum well heterostructure. Unlike other semiconductor devices, where the optical transition occurs between conduction and valence band, in quantum cascade lasers (QCLs) the desired transition frequency and other optical and electrical properties such as the dipole moment or electron transport can be designed by adjusting the thickness of the corresponding barrier and well layers. By selecting a well-suited material system, both the mid-infrared (mid-IR) and terahertz (THz) region become accessible. QCLs with a broadband optical emission spectrum are suitable for the generation of optical frequency combs, i.e., laser spectra consisting of perfectly equidistant and phase-locked lines. In both mid-IR and THz regimes, the generation of optical frequency combs with QCL sources was

already demonstrated.[1,2] In principle, the gain spectrum of these devices can be very broadband, potentially covering one frequency octave and, therefore, pointing toward self-referenced emission.[3–5] However, the mode-locked comb emission is usually restricted to a rather small dynamic range at low current densities. Here, the small group velocity dispersion (GVD) allows the four-wave-mixing processes to effectively lock the cavity modes without the need of external optical elements. Mode-locking over the entire 1.3 THz gain bandwidth and across more than 60% of the operational range of a heterogeneous QCL device has been achieved recently by altering its intracavity light intensity.[6] This has been done by reducing the reflectivity of the device back facet to induce higher mirror losses through coating with an epitaxially grown multilayer graphene film. Moreover, the extremely accurate frequency resolution recently demonstrated by these miniaturized combs when externally phase referenced[7] shows their enormous potential in the area of metrology and spectroscopy and makes QCL devices highly interesting for integration into innovative applications of different fields, e.g., astronomy or healthcare diagnostics.[8] In recent years, a main focus of research has been dedicated to the reconstruction of time domain profiles and intermodal phase relations of QCL frequency combs. Based on methods such as the shifted-wave interference Fourier-transform spectroscopy (SWIFTS)[9,10] or the Fourier-transform analysis of comb emission (FACE),[7,11,12] the phase stability of the frequency combs could be demonstrated. The coexistence of frequency modulated (FM) and amplitude modulated (AM) comb regimes in both mid-IR and THz QCL sources was experimentally retrieved[9,10,13] and could be replicated in several theoretical studies based on different simulation models.[14–19]

To access and close the THz gap between microwaves and optics, the QCL is the ideal semiconductor laser source. One major disadvantage of direct THz light generation with QCL sources is the lack of devices operating at room temperature resulting from the complexity of establishing and preserving population inversion between the upper and lower laser levels.[20] This problem arises since the THz photon energy is around a few meV and thus well below the thermal energy of 26 meV at room temperature. The laser system tends to thermodynamic equilibrium and intrinsically destroys population inversion. Until very recently, the requirement of cryogenic cooling for direct THz QCL operation could only be overcome by THz difference frequency generation (DFG).[21,22] However, the development of THz QCL designs with a maximum operating temperature exceeding 200 K in pulsed operation opened the door for device applications using less demanding cooling systems, e.g., thermoelectric Peltier cooling.[23,24] As the aforementioned devices do not work in continuous-wave (CW) operation, and the maximum CW operation temperature of THz designs is limited to 129 K,[25,26] we focus in the following on an alternative approach to generate CW THz radiation without cryogenic cooling or even at room temperature by intracavity DFG in dual-wavelength mid-IR QCL sources. Belkin *et al.*[27] presented the first so-called THz DFG-QCL device in 2007, and since then great effort has been put into the engineering and development of such devices.[22,28–30] The main advantage here is that no population inversion for THz transition is required, and room temperature operation with such dual-wavelength mid-IR QCLs is well accessible. In Fig. 1(a), the basic working principle of a THz DFG-QCL is described. Optical transition of electrons by stimulated emission

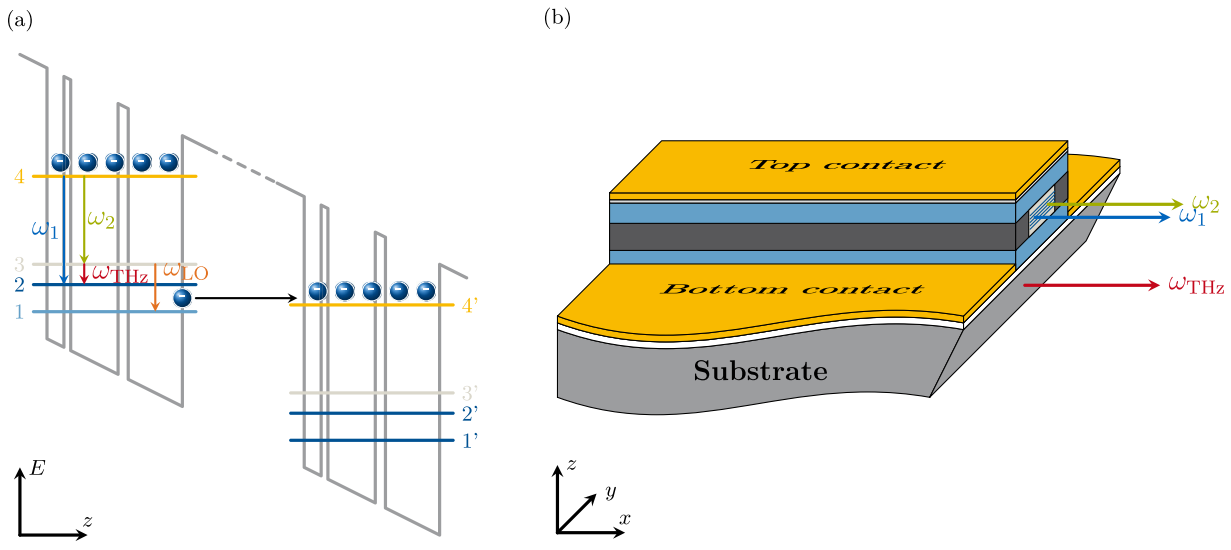

FIG. 1. Mid-IR pump frequencies are indicated by ω_2 (green) and ω_1 (blue), and THz emission is represented by ω_{THz} (red). (a) Schematic of the DFG process between the quantized electron states in the conduction band profile of a QCL. The energy levels (4,3,2) form a DFG triplet, and electron extraction is illustrated by LO phonon scattering into level 1 followed by injection into the adjacent period. (b) Schematic of a THz DFG-QCL waveguide with mid-IR emission outcoupled through the laser active region facets, and THz emission emitted into the semi-insulating InP substrate utilizing a Cherenkov phase-matching scheme to obtain efficient THz radiation extraction.

from the upper laser level 4 to the lower laser levels 3 and 2 occurs, and lasing starts at two mid-IR pump modes ω_1 and ω_2. A THz mode at frequency ω_{THz} results from the nonlinear mixing process and downconversion of mid-IR frequencies ω_1 and ω_2. Here, the DFG triplet is formed by three states 4, 3, and 2. Subsequently, efficient depopulation is achieved by longitudinal optical (LO) phonon scattering to level 1 and is followed by injection into the upper laser level 4′ of the adjacent period. The active region has to be designed with a large second-order nonlinear susceptibility to obtain an efficient THz DFG process. Quantum engineering of the QCL active region toward giant nonlinearities is strongly dependent on the coupling of the involved triplets of states. By utilizing a dual-upper state (DAU) active region design instead of a stacked bound-to-continuum (BTC) structure, a stronger nonlinearity due to additional DFG triplet states is obtained while keeping the gain spectrum comparably broad.[31–34]

The first THz DFG-QCLs consisted of a single waveguide with modal phase matching for both mid-IR and THz frequencies and, thus, suffered from excessive absorption in the THz regime.[27,28,35] To overcome this inefficiency in the outcoupling of THz radiation, QCL waveguides with a Cherenkov phase-matching scheme were introduced and are now standard for THz DFG-QCL devices.[31,36,37] Here, the mid-IR pump modes are confined in the laser active region and are outcoupled through the mid-IR waveguide facets, whereas THz emission is directed toward the semi-insulating (SI) InP substrate, providing comparably low THz loss. Cherenkov emission into the substrate is achieved, when the phase-velocity of the nonlinear polarization wave within the slab waveguide is faster than in the surrounding medium. As the SI InP provides a higher THz refractive index n_{THz} than the group effective refractive index n_{g} of the pump modes, the THz radiation exits the active region under the Cherenkov emission angle[22] $\theta_{\mathrm{c}} = \cos^{-1}(n_{\mathrm{g}}/n_{\mathrm{THz}})$. To avoid internal reflection of Cherenkov wave emission at the substrate/air interface, the front facet has to be polished at an angle between 20° and 30°.[22,28–30] The schematic of such a Cherenkov THz DFG-QCL waveguide is illustrated in Fig. 1(b).

Initially, the main research focus was laid on the development and fabrication of widely tunable THz DFG-QCL emission with narrow linewidth in the frequency range of 1–6 THz.[33,38–43] Here, broadband tuning is obtained either by external-cavity (EC) DFG-QCL setups[41–43] or by monolithic electrically tunable THz DFG-QCLs.[33,38–40] Single-mode THz operation is established by dual-period or sampled distributed feedback (DFB) grating approaches with dual-wavelength single mid-IR pump modes.[28,39,41] Furthermore, the applicability for high-precision spectroscopy was tested by characterizing the spectral purity and tunability.[44,45] Recently, broadband THz DFG-QCL frequency combs were generated by mixing a single mid-IR mode, which is selected by an integrated largely frequency detuned DFB grating, and a frequency comb centered at a second mid-IR frequency in a multimode Fabry–Perot (FP) cavity.[22,32,46–48] This distributed feedback/Fabry–Perot configuration for nonlinear THz DFG-QCL frequency comb generation is schematically illustrated in Fig. 2.

To model the nonlinear mixing process in QCLs, Maxwell–Bloch equations (MBEs) are a valuable tool, as they offer a relatively compact and numerically efficient model.[49,50] The evolution of the quantum system is described by the Bloch equations, which are

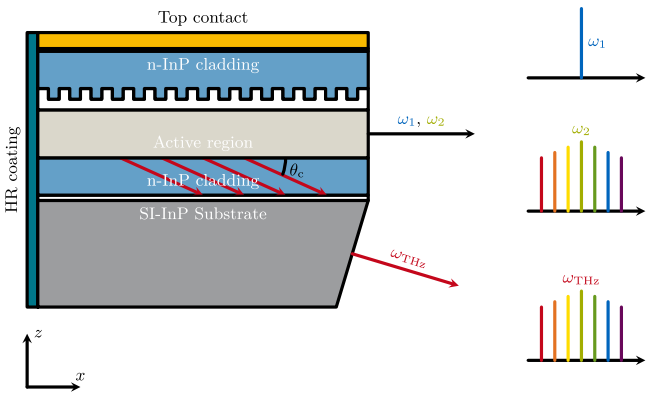

FIG. 2. Schematic of a distributed feedback/Fabry–Perot configuration for nonlinear THz DFG-QCL frequency comb generation. The buried DFB grating is etched into the upper guide layer, which results in a single DFB mode ω_1 frequency detuned from the gain maximum. The FP frequency comb is centered around ω_2, and the THz comb radiation generated by nonlinear mixing is extracted into the substrate, where it gets outcoupled through the polished facet. The back facet is coated with a high-reflection (HR) coating.

coupled to Maxwell's equations for the classical description of the optical field. Among other active photonic devices,[50–53] the MBE framework has been applied extensively to QCLs, especially for the dynamical simulation of mode-locking,[12,54–58] the investigation of coherent instabilities,[17,59–61] and the formation of fundamental and harmonic frequency comb regimes.[15,16,62–68] In this context, it is useful to sub-divide these works into different types of simulation approaches, based on standard Maxwell–Bloch equations,[12,14,55,57–65,68] effective semiconductor Maxwell–Bloch equations (ESMBEs),[15,16,56] or related (semi-)analytical models.[14,17,54,66–68] The ESMBEs are a special type of MBEs consisting of a two-level system that interacts with an electric field. Advanced effects, like the linewidth enhancement factor, are here included to take into account an asymmetric gain profile and to provide an improved description of all nonlinear optical key features, such as four-wave mixing due to the Kerr effect. For a detailed comparison between ESMBEs and MBEs, the reader is referred to the recent review paper about frequency combs in QCLs.[69] The work presented here is based on the open-source solver tool mbsolve,[58,65,70–72] where the generalized one-dimensional MBEs are treated without invoking rotating wave approximation (RWA). This detailed model is crucial for the simulation of THz DFG-QCL frequency comb setups, as the spectrum spans from the THz region to the mid-IR regime and cannot be resolved within the RWA. Referring to the original Bloch equations for a two-level system, our generalized Maxwell–Bloch model can be extended to multiple levels. Nonlinear and nonclassical effects, like tunneling processes and coherence of the relevant optical transitions, may account for an asymmetric gain and are here included in the system Hamiltonian. Furthermore, we extract all required parameters for the description of the quantum system self-consistently from our in-house ensemble Monte Carlo (EMC) approach for stationary carrier transport simulations.[73,74]

The paper is structured as follows: Our self-consistent multi-domain simulation approach, consisting of EMC-based stationary carrier transport modeling coupled to dynamical simulations based on open-source Maxwell–Bloch solver mbsolve, is introduced in Sec. II. In Sec. III, we present simulation results for two different THz DFG-QCL setups and validate them against experimental data. The paper is concluded in Sec. IV.

II. SIMULATION MODEL

For spatiotemporal simulations of THz DFG-QCL frequency combs, we use a self-consistent multi-domain approach. To model the light–matter interaction in a DFG-QCL, our open-source Maxwell–Bloch tool mbsolve is used.[65,75] All input parameters required for a complete description of the quantum system are extracted from our in-house Monaco framework, a quantum cascade (QC) device simulation tool.[73,74,76,77] In the following, the Monaco framework with the base library for QC device specifications and the charge carrier transport simulation approach as well as the mbsolve framework for dynamic full-wave Maxwell–Bloch simulations of coherent light–matter interaction in QCL structures are explained in more detail.

A. Device description and carrier transport simulations

The Monaco framework consists of an object-oriented device engineering tool for QC structures and includes different modules.[76] A setup library for the description of the QC active region and simulation parameters is provided. Here, all the important information about the active gain medium is specified, i.e., the active region period consisting of the layer collection with barrier and well materials. Furthermore, relevant parameters of the waveguide model, e.g., the cavity length L, the linear loss term α_0, the facet reflectance R, and the confinement factor Γ, are defined. Other relevant environmental simulation parameters, e.g., applied bias V and temperature T, describe the simulation scenario.

To obtain realistic simulation results, an accurate and detailed description of the specific physical properties of the used III–V compound semiconductor material systems is required. Environmental influences such as temperature or strain on the semiconductor lattice can have significant impact and have to be taken into account for the calculation of specific material parameters such as the energy bandgap E_g or the effective mass m^*. An exact determination of the conduction band discontinuity in the quantum well heterostructure is important for the calculation of eigenenergies E_i and wavefunctions ψ_i of the QCL laser system. Hence, to characterize the semiconductor band structure and the conduction band discontinuities in the quantum well heterostructure, we apply the model-solid theory.[78] It is based on density-functional calculations, where the individual bulk semiconductors are described by *ab initio* pseudopotenials. The calculated band energies are aligned on absolute energy values, which makes it possible to calculate conduction band offsets (CBOs) by subtracting the conduction band edge energies of individual well and barrier materials. As bandgap values in the density-functional theory cannot be predicted correctly, the experimentally measured bandgap values are used to get a more precise solution of the band structure.[79] Effects on the band structure due to pseudomorphic strain are intrinsically included in the model-solid theory. For the development of short-wavelength QCLs beyond the CBO limit of 0.52 eV in lattice-matched systems, the material composition of the mid-IR QCL material system InGaAs/InAlAs has to be strain engineered. The DFG-QCL designs investigated in this paper are also based on strain-compensated InGaAs/InAlAs material systems to reduce the thermally activated carrier leakage to continuum states above the barrier potentials and thereby increase the device performance.[33] The composition of strain-compensated QCL heterostructures during the growth process has to be selected carefully to avoid relaxation defects in the semiconductor lattice. This is achieved by balancing compressive and tensile strain of well and barrier materials. The relative shift in conduction band energy due to hydrostatic strain is given by[78]

$$P_\epsilon^c = \Delta E_c = a_c \frac{\Delta\Omega}{\Omega}, \tag{1}$$

where a_c is the hydrostatic deformation potential of the conduction band. The volume change arising from bi-axial strain $\Delta\Omega/\Omega = \mathrm{Tr}(\vec{\epsilon}) = 2\epsilon_\parallel + \epsilon_\perp$ is calculated by the trace of the strain tensor $\vec{\epsilon}$. In a similar manner, the change in valence band position is obtained by[78]

$$P_\epsilon^v = \Delta E_v = a_v \frac{\Delta\Omega}{\Omega}, \tag{2}$$

with the hydrostatic deformation potential a_v of the valence band. The effective bandgap energy under strain influence is then given by $E_g^s = E_g + P_\epsilon^c + P_\epsilon^v$. In Fig. 3(a), the CBO of the material system InAlAs/InGaAs on InP for $x \in [0, 1]$ is depicted. As can be seen here, the material composition choice of $In_xAl_{1-x}As$ has a significant influence on the material system CBO value, whereas the indium concentration variation in $In_xGa_{1-x}As$ does not affect the CBO value considerably. In QCL device engineering, it would make sense to tune the target CBO value by $In_xAl_{1-x}As$ composition and balance the strain in the active period by adjusting the indium concentration of the $In_xGa_{1-x}As$ well materials.

Sugawara *et al.*[80] investigated the effects of strain on the effective mass at the conduction band edge and derived a model based on an 8-band $\mathbf{k}\cdot\mathbf{p}$ theory for the calculation of effective masses in strained materials. Here, it was demonstrated that the electron effective mass at the conduction band edge becomes anisotropic for $In_xGa_{1-x}As/InP$ quantum wells. The effective mass for growth direction $m_\perp^*$ and in-plane $m_\parallel^*$ effective mass at the conduction band edge are calculated with[80]

$$\frac{1}{m_\parallel^*} = \frac{1+2F}{m_0} + \frac{2\mathbf{P}^2}{3}\left[\frac{(\sqrt{2}\alpha-\beta)^2}{E_g + P_\epsilon^c - E_{LH}} + \frac{(\sqrt{2}\beta+\alpha)^2}{E_g + P_\epsilon^c - E_{SO}}\right], \tag{3a}$$

$$\frac{1}{m_\perp^*} = \frac{1+2F}{m_0} + \frac{\mathbf{P}^2}{3}\left[\frac{3}{E_g + P_\epsilon^c - E_{HH}} + \frac{(\sqrt{2}\alpha+\beta)^2}{E_g + P_\epsilon^c - E_{SO}} + \frac{(\alpha-\sqrt{2}\beta)^2}{E_g + P_\epsilon^c - E_{LH}}\right], \tag{3b}$$

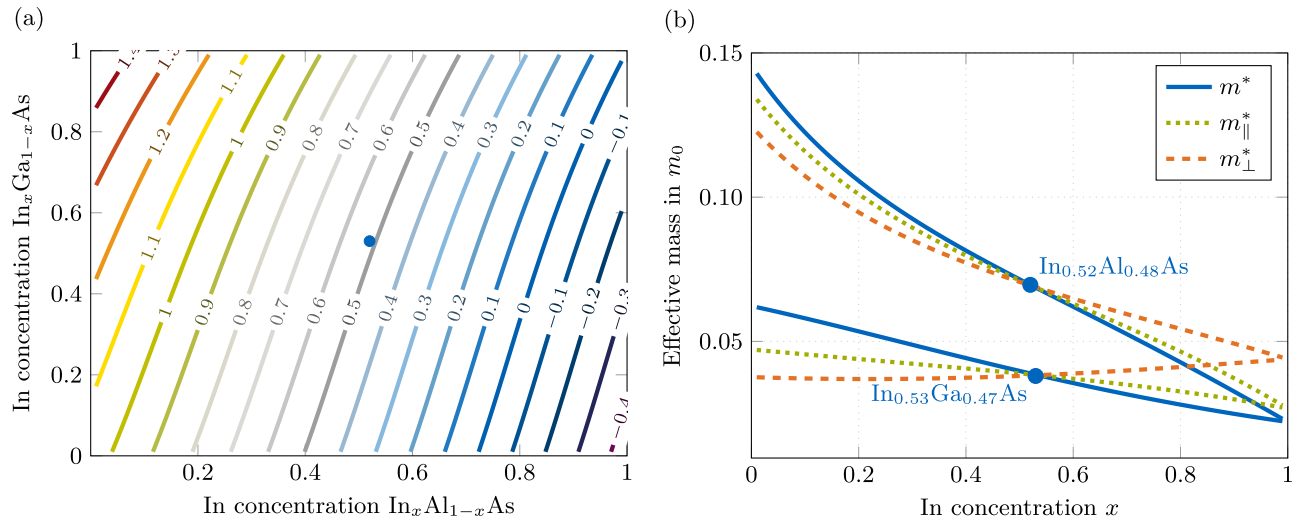

FIG. 3. Calculated strain effects for the material system InGaAs/InAlAs at 300 K on an InP substrate with (001) orientation. (a) Contour plot of the CBO of the $In_xGa_{1-x}As/In_xAl_{1-x}As$ material system for indium (In) concentrations $x \in [0, 1]$. The lattice-matched material system $In_{0.52}Ga_{0.48}As/In_{0.53}Al_{0.47}As$ is represented by the blue dot. (b) Effective mass m^* at the Γ-point of the materials $In_xGa_{1-x}As$ and $In_xAl_{1-x}As$ for $x \in [0, 1]$. Strain effects leads to an anisotropic effective mass with different values for growth direction $m^*_\perp$ and in-plane $m^*_\parallel$ values.

where m_0 is the electron mass, F is the Kane parameter, $\mathbf{P}$ is the momentum matrix element between the conduction and valence band, E_g is the bandgap energy without strain contributions, and E_{SO}, E_{HH}, and E_{LH} are the band edge energies of split-off, heavy hole, and light hole bands. The two variables α and β represent the strain influence. In the case of lattice-matched material systems with $\alpha = 1$, $\beta = 0$, and $E_{HH} = E_{LH} = E_v = 0$, we obtain an isotropic effective mass at the band edge ($m^*_\perp = m^*_\parallel$), and the effective mass calculation gets reduced to the simplified formula,[79]

$$\frac{1}{m^*} = \frac{1+2F}{m_0} + 2\mathbf{P}^2 \frac{E_g + 2\Delta_{SO}/3}{E_g(E_g + \Delta_{SO})}, \tag{4}$$

with $\Delta_{SO} = E_{LH} - E_{SO} = -E_{SO}$. Effective mass m^* calculations at the conduction band edge for materials $In_xGa_{1-x}As/In_xAl_{1-x}As$ on an InP substrate at $T = 300$ K are illustrated in Fig. 3(b). Biaxial strain leads to a breakdown of the isotropy in effective mass. Moving away from the lattice-matched system $In_{0.52}Al_{0.48}As$ and $In_{0.53}Ga_{0.47}As$ on InP results in a divergence of effective mass for growth direction and in-plane effective mass with varying indium concentrations.

Another effect to be considered in the simulation of QCLs is the breakdown of the parabolic dispersion relation between energy and wavenumber in the conduction band of semiconductor materials for higher energy levels. The nonparabolicity effects are treated within the $\mathbf{k}\cdot\mathbf{p}$ perturbation theory, where an energy-dependent effective mass is obtained. The energy-dependent effective mass based on 14-band $\mathbf{k}\cdot\mathbf{p}$ calculation is given by[81]

$$m^*_\perp(E) = \frac{m^*_\perp(0)}{2\alpha' E}\left[1 - (1 - 4\alpha' E)^{\frac{1}{2}}\right], \tag{5a}$$

$$m^*_\parallel(E) = m^*_\parallel(0)[1 + (2\alpha' + \beta')E], \tag{5b}$$

with nonparabolicity parameters α' and β'.[73] Approximately, we can write $\alpha' = \left(E_g + \Delta_{SO}/3\right)^{-1}$.

Taking into account all important parameters in our device description, the corresponding wavefunctions ψ_i and the system Hamiltonian $\hat{H}_s$ are calculated within an object-oriented Schrödinger–Poisson (SP) solver library. The numerical approach used for solving the Schrödinger equation is based on the transfer matrix method.[73,82] Additionally, a solver for the Poisson equation takes care of the mean-field treatment of the electron–electron interaction and determines the additional electrostatic potential. As basis for the SP solver, extended states,[73] tight-binding states,[74] or EZ-states[83] can be specified. (Here, the term EZ refers to energy E and position z within the subspace of the multiplet.) The equation system is solved iteratively until convergence is reached. The quantum mechanical description comprising wavefunctions, Hamiltonian, and averaged effective masses of subbands, together with the total potential resulting from the conduction band profile and band bending effects due to space charges, can be extracted and serve as input data for the multidomain simulation approach.

Our carrier transport simulation model is based on the EMC method, a self-consistent 3D approach taking into account all necessary intersubband processes.[73] The scattering-induced transport of electrons between quantized levels is modeled semiclassically by evaluating the Boltzmann equation. Here, all relevant mechanisms such as LO and acoustic phonon, electron–electron, impurity, interface roughness, and alloy scattering are considered. The corresponding rates are calculated self-consistently at the beginning of the simulation using Fermi's golden rule. For the initialization of simulation, an ensemble of electrons is distributed over the

different states characterized by the subband index i and in-plane wavevector $\mathbf{k}$. According to the Monte Carlo method, the QCL system will converge to the stationary solution by stochastically evaluating the scattering events. To overcome the lack of quantum coherence and quantum mechanical dephasing mechanisms, the EMC model was extended by essential quantum correction terms.[74] The density-matrix EMC (DM-EMC) approach includes elements of the density matrix formalism to account for tunneling across thick injection barriers, described by the Rabi frequencies $\Omega_{ij} = \langle\psi_i|\hat{H}_s|\psi_j\rangle/\hbar$.[73,74,83] Here, $\hbar$ is the reduced Planck constant.

By analyzing the stationary carrier transport simulation results, a reduced and accurate description of the quantum system can be found and is saved in a Python script, which serves as input for mbsolve simulations.[65] The quantum mechanical description comprises the level occupations ρ_{ii}, system Hamiltonian $\hat{H}_s$ with eigenenergies E_i and anticrossing energies $\hbar\Omega_{ij}$, dipole moment operator $\hat{d}_z$, dephasing rates Γ_{ij}, and scattering rates r_{ij}. Here, the important tunneling and relevant optical transitions for favored mid-IR (ω_1, ω_2) and THz (ω_{THz}) frequencies have to be taken into account. For the one-dimensional dynamic Maxwell–Bloch simulations, the energy-resolved dephasing rates extracted from EMC have to be averaged over the population inversions of the involved subbands, as it is described in detail in Refs. 63 and 74.

B. Generalized Maxwell–Bloch equations in 1D

In our simulation platform, the light–matter interaction is treated by full-wave Maxwell–Bloch equations, where a quantum mechanical description for the electron dynamics and a classical description for the optical field is used. Here, the density matrix $\hat{\rho}$ and its interaction with the environment are described by the Lindblad equation, the general form of a time-local and Markovian linear master equation for quantum systems, which can be written as

$$\partial_t\hat{\rho} = -\mathrm{i}\hbar^{-1}\left[\hat{H}_s - \hat{d}E_z, \hat{\rho}\right] + \hat{\rho}_{\mathrm{diss}}. \tag{6}$$

The Hamiltonian $-\hat{d}E_z$ describes the interaction of laser levels with optical field E_z. The dissipation superoperator $\hat{\rho}_{\mathrm{diss}}$ displays the interaction with the environment and is here described by scattering and dephasing rates, r_{ij} and Γ_{ij}. Further levels can be considered in Eq. (6), and additional effects such as tunneling are inherently included in the system Hamiltonian $\hat{H}_s$.

Maxwell's equations capture the optical propagation through the waveguide resonator. To minimize the numerical load of the simulations, we exploit a one-dimensional model, which is justified for optical field propagation in waveguides with invariant transverse field distribution.[50] The time evolution of the magnetic field H_y and the electric field E_z is given by

$$\partial_t E_z = (\varepsilon_0\varepsilon_{\mathrm{r},\infty})^{-1}\left(-\sigma E_z - \sum_i \partial_t P^i_{z,\mathrm{class}} - \Gamma\partial_t P_{z,\mathrm{qm}} + \partial_x H_y\right), \tag{7a}$$

$$\partial_t H_y = \mu^{-1}\partial_x E_z, \tag{7b}$$

where $\varepsilon_0\varepsilon_{\mathrm{r},\infty}$ is the product of the vacuum permittivity and the relative permittivity at high frequencies, σ is the material conductivity, and $\sum_i \partial_t P^i_{z,\mathrm{class}}$ is the sum of polarization terms accounting for GVD in dispersive media.[70,72,84] Taking into account the dipole moment of the quantum system, the macroscopic polarization term $P_{z,\mathrm{qm}}$ is described by

$$P_{z,\mathrm{qm}} = n_{3\mathrm{D}}\mathrm{Tr}\left\{\hat{d}_z\hat{\rho}\right\}, \tag{8}$$

where $n_{3\mathrm{D}}$ is the charge carrier density. Equations (6) and (7) constitute a semiclassical model for the simulation of spatiotemporal dynamics in DFG-QCL devices. Detailed information about the macroscopic Maxwell–Bloch equation system and the mbsolve tool can be found in Refs. 50 and 65.

To simulate open radiation problems in mbsolve, we use perfectly matched layer (PML) absorbing boundary conditions, introduced by Berenger.[85] Much attention has been drawn to the improvement and generalization of PMLs. One of these works was conducted by Fang and Wu,[86] who proposed the so-called generalized PMLs (GPMLs) that can, in contrast to the standard form, also be matched to lossy media. Gedney[87,88] first used an uniaxial anisotropic medium to derive the PMLs and hereby gave them a physical interpretation.

To improve the absorbing characteristics of open radiation simulations in mbsolve, a modified PML model was implemented.[72] Parasitic reflection errors at the boundary arising from an impedance mismatch due to the interaction with the internal quantum system could be suppressed by expanding the active QCL gain medium into the PML region. In addition, we have developed partially reflecting layer (PRL) boundary conditions,[89] which model the reflectance R at the facet of our THz DFG-QCL frequency comb device correctly without decreasing the simulation performance by adding surrounding layers at the active gain medium facets. It is important to emphasize here the necessity of PRLs for correct light outcoupling ($R < 1$) at the facet. A spatially averaged loss would impose an unrealistically strong attenuation on the DFB mode, which counteracts the optical feedback mechanism. Thus, single-mode operation would be suppressed, and DFG mixing and THz comb generation would not be feasible. These boundary conditions are based on the modified PMLs.[72] Unlike in PML absorbing boundaries, we here introduce an impedance mismatch at the interface of the active region and the PRL. The facet reflectance R is adjusted by the relative permeability of the artificial boundary material, i.e.,

$$\mu_{\mathrm{r,PRL}} = \mu_{\mathrm{r}} \cdot \left(\frac{1 \pm \sqrt{R}}{1 \mp \sqrt{R}}\right)^2, \tag{9}$$

where μ_{r} is the relative permeability of the material at the truncation facet.

III. RESULTS AND DISCUSSION

In the following, we present simulation results for two different THz DFG-QCL setups. One setup consists of a single-phonon

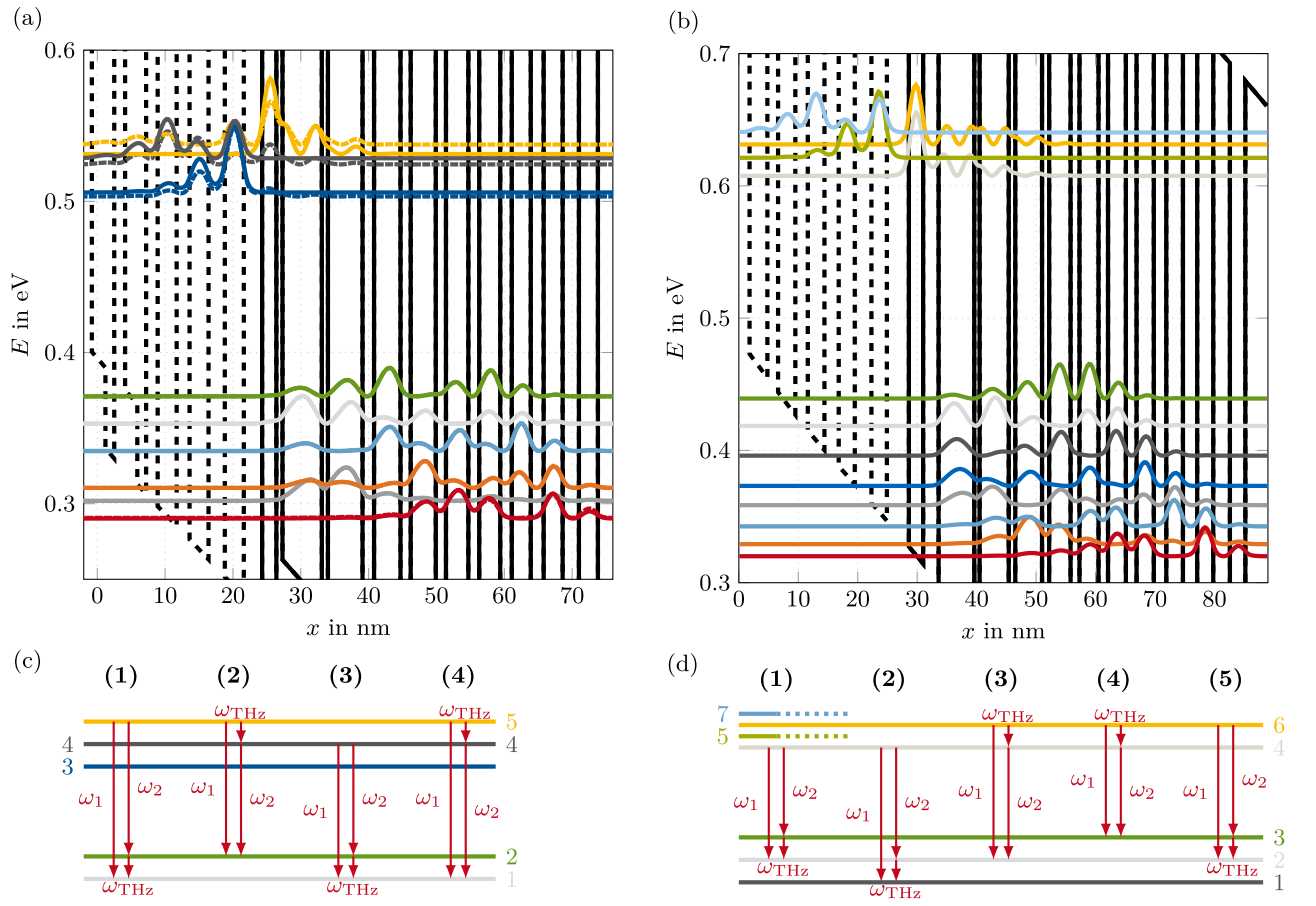

FIG. 4. Investigated conduction band profiles and probability densities of the two modeled THz DFG-QCL structures. (a) Single-phonon resonance depopulation scheme based on a strain-balanced $In_{0.37}Al_{0.63}As/In_{0.65}Ga_{0.35}As/In_{0.53}Ga_{0.47}As$ material system at a lattice temperature of 293 K.[33] The layer sequence (in nm) of one period is **2.7**/ 2.1/ **0.9**/ *3.2*/2.6/ **0.9**/ *3.0*/ 2.1/ **1.7**/ *2.4*/ 1.5/ **1.5**/ *2.2*/ 1.5/ **1.5**/ *2.0*/ 1.3/ **1.6**/ *1.8*/ 1.3/ **1.7**/ 2.8/ **1.9**/ 2.8/ **2.4**/ 2.8, barriers are in boldface, well layers with $In_{0.53}Ga_{0.47}As$ are highlighted in italic, for the underlined layers a doping density of 1.7×10^{17} cm^{-3} (n-type) is assigned, and the applied bias is 50 kV cm^{-1}. Here, tight-binding (solid lines) and extended states (dashed lines) are illustrated. (b) Band structure of the dual-upper state active region based on a strain-compensated $In_{0.6}Ga_{0.4}As/In_{0.44}Al_{0.56}As$ material system at a lattice temperature of 78 K.[34] The layer sequence (in nm) of one period is **3.7**/2.4/**2.6**/6.0/**0.9**/4.9/**1.1**/4.5/**1.2**/3.6/**1.5**/3.2/**1.6**/3.0/**1.8**/2.9/**2.1**/2.8/**2.4**/2.7/**2.8**/2.6, n-doped layers (Si, 1×10^{17} cm^{-3}) are underlined. The applied bias is here 56 kV cm^{-1}. (c) Schematic description of the DFG processes in the single-phonon resonance depopulation structure 4(a). (d) Schematic description of the DFG processes in the dual-upper state active region 4(b).

resonance depopulation (SPR-depopulation) structure,[33] whereas the other setup is based on a dual-upper state active region.[34] The conduction band profile together with the probability densities of the wavefunctions for both QCL setups are illustrated in Fig. 4. For a complete characterization of the electrical and optical properties, we divide this section into two parts: First, we present stationary charge carrier transport simulations of the given structures based on the EMC method[73] and compare them with the corresponding experimental data.[33,34,90] Second, dynamic simulations of the light–matter interaction using the open-source Maxwell–Bloch simulation tool mbsolve are provided. Here, we can reproduce the experimentally obtained results and demonstrate THz frequency comb generation in DFG-based QCLs by self-consistent modeling.[47,48]

A. Stationary carrier transport simulations

To classify the efficiency of the nonlinear mixing process and the potential for broadband THz comb emission, we investigate the gain spectrum in the mid-IR regions and characterize the strength of the nonlinearity in the active gain region. Here, the optical gain is calculated by[73]

$$g(\omega) = \frac{\omega}{\varepsilon_0 c_0 n_{\text{eff}}} \sum_{i,j} d_{ij}^2 \frac{\Gamma_{ij}}{\Gamma_{ij}^2 + \left(\hbar\omega - \hbar\omega_{ij}\right)^2} \left(N_i - N_j\right), \tag{10}$$

where c_0 is the vacuum speed of light, n_{eff} is the effective refractive index, and $d_{ij} = -ez_{ij} = -e\langle\psi_i|\hat{z}|\psi_j\rangle$ is the dipole matrix element with elementary charge e and position operator $\hat{z}$. Moreover, $\hbar\omega_{ij} = \left(E_i - E_j\right)$

denotes the resonance energy between level i and j, and N_i is the population density of level i. The transition linewidth broadening is given by[74]

$$\Gamma_{ij} = (\gamma_i + \gamma_j)/2 + \gamma_{ij,\mathrm{p}}, \tag{11}$$

where γ_i corresponds to level broadening of level i and $\gamma_{ij,\mathrm{p}}$ represents the pure dephasing contribution.

The second-order nonlinear susceptibility $\chi^{(2)}$ is calculated by[91]

$$\begin{aligned}\chi^{(2)}(\omega_{\mathrm{THz}} = \omega_1 - \omega_2) = -\frac{e^3}{\varepsilon_0}\sum_{i,j,k} N_i z_{ij} z_{jk} z_{ki} \Bigg\{ &\left[\frac{1}{(\hbar\omega_{ki} - \mathrm{i}\Gamma_{ki} - \hbar\omega_{\mathrm{THz}})} + \frac{1}{\hbar\omega_{kj} + \mathrm{i}\Gamma_{kj} + \hbar\omega_{\mathrm{THz}}}\right] \\ &\times \left[\frac{1}{(\hbar\omega_{ji} - \mathrm{i}\Gamma_{ji} + \hbar\omega_2)} + \frac{1}{\hbar\omega_{ji} - \mathrm{i}\Gamma_{ji} - \hbar\omega_1}\right] - \left[\frac{1}{(\hbar\omega_{kj} - \mathrm{i}\Gamma_{kj} - \hbar\omega_{\mathrm{THz}})} + \frac{1}{\hbar\omega_{ki} + \mathrm{i}\Gamma_{ki} + \hbar\omega_{\mathrm{THz}}}\right] \\ &\times \left[\frac{1}{(\hbar\omega_{ij} - \mathrm{i}\Gamma_{ij} + \hbar\omega_2)} + \frac{1}{\hbar\omega_{ij} - \mathrm{i}\Gamma_{ij} - \hbar\omega_1}\right]\Bigg\},\end{aligned} \tag{12}$$

where the levels with indices i, j, k build a DFG triplet. Here, all combinations of involved upper and lower laser levels are taken into account. A detailed and more sophisticated Monte Carlo analysis of the second-order nonlinear susceptibility can be found in the literature (Refs. 91 and 92), where also the effects of the intrasubband kinetic electron distribution were included. By taking into account only the dominant DFG triplets near resonance to the mid-IR design frequencies ω_1 and ω_2, a significantly reduced number of terms in Eq. (12) remains.[21,33,41,91]

1. Single-phonon resonance depopulation structure

The modeled THz DFG-QCL design consists of a SPR-depopulation structure emitting at $\lambda \sim 7.8\,\mu\mathrm{m}$ and is based on strain-balanced InGaAs/InAlAs; experimental data can be found in Refs. 33 and 47. At the operation temperature of 293 K, a CBO of 740 meV was specified in literature[33] and is used in this paper for the calculation of wavefunctions. Here, we investigate the THz DFG-QCL device for two potential approaches, as it is illustrated in Fig. 4(a). On the one hand, we use a tight-binding potential V_{tb} for the calculation of nine wavefunctions per period giving rise to one upper laser level and three lower laser levels. Injection of charge carriers into the upper laser level is modeled here by resonant tunneling from two injector states of the adjacent period. The calculated coupling strengths of the two narrowest anticrossed pairs of tunneling states are $2\hbar\Omega_{45} = 14$ meV and $2\hbar\Omega_{35} = 17.8$ meV, which are in good agreement with the coupling strength $2\hbar\Omega = 16.5$ meV determined in the experimental paper (Ref. 33). Notably, tunneling transitions fully contribute to the DFG process in dynamic Maxwell–Bloch simulations. However, no predictions about their contributions to the second-order nonlinear susceptibility can be made within the tight-binding approach, as the dipole moments d_{45} and d_{35} are insignificantly small due to the strong localization of the states to the left and right of the injection barrier. It is important to take into account also the extended state approach for the characterization of the nonlinear susceptibility, since it was proposed in the experimental paper (Ref. 33) that the injector levels can have a substantial impact on the DFG process. With the actual potential V, we can determine the extended states. One of the injector states in the tight-binding approach now acts as an additional upper laser level. The lower laser levels as well as the depopulation miniband for the actual potential V do not change significantly in position and probability densities in comparison to the corresponding tight-binding levels. For the carrier transport simulations of the SPR-depopulation QCL design, an average interface roughness height $\Delta = 0.06$ nm is selected to obtain realistic simulation results.[93] With the interface parameter product $\Delta\Lambda \approx 1\ \mathrm{nm}^2$, which is the experimental estimate for the InGaAs/InAlAs material system,[94,95] a correlation length of $\Lambda = 16.67$ nm is calculated.

In Fig. 5(a), the normalized gain curve from the EMC simulation for tight-binding as well as extended states and the experimentally measured electroluminescence (EL) curve from Ref. 33 are illustrated. We obtain simulated linewidth values of ~412 and ~442 cm^{-1} for tight-binding states and extended states, respectively. The experimentally measured linewidth of ~380 cm^{-1} is slightly narrower; however, the EL measurement was performed at higher bias compared to the simulation. The bias change gives rise to varying lasing channels; thus, the dominant optical transition in the simulation is $5 \rightarrow 1$, while in the EL setup $4 \rightarrow 2$ is the dominant optical transition. The applied QCL bias in this paper is adjusted for efficient THz DFG-QCL comb generation and is derived from P–I–V characterization given in Ref. 47. In addition, we see a small blue shift of simulated curves with respect to the measured spectrum, although calculated wavefunctions and eigenstates are in good agreement with the ones shown in Ref. 33 at the given bias of 65 kV cm^{-1}. Minor inaccuracies in the calculation of simulation parameters, e.g., CBO, could arise with the natural limitation of our theoretical model. On the other hand, small deviations could also stem from process uncertainties during the fabrication, i.e., layer thickness variations, we cannot account for in the simulation.[96]

In Fig. 5(b), the level broadening γ_i and the relative level occupation ρ_{ii} in the relevant period are shown as a function of the subband energy. We obtain a similar thermalized behavior of relative level occupations in the lower lying levels for both approaches. Level 3 acts as an efficient injector to upper laser level 5 in the tight-binding approach, whereas in the extended state

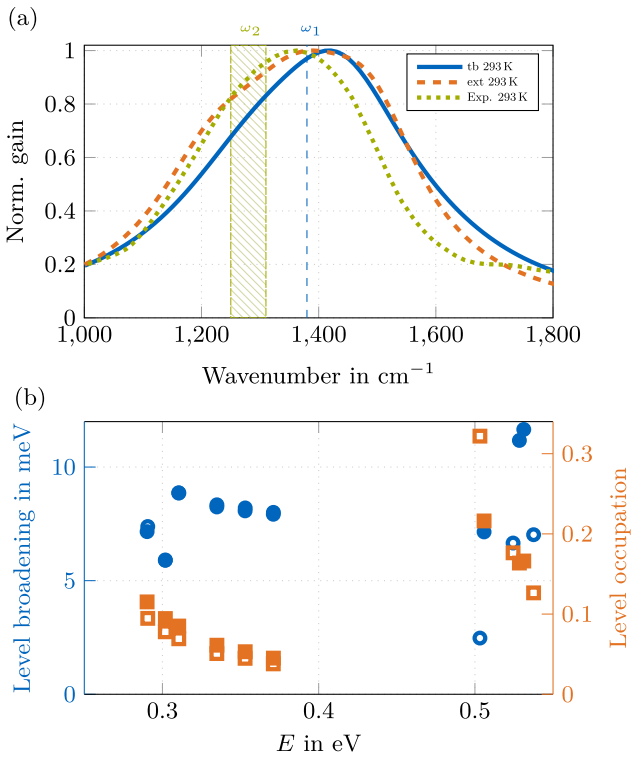

FIG. 5. Simulation results of the SPR-depopulation design. (a) Normalized gain vs wavenumber for simulated tight-binding (tb) (solid line) and extended (ext) states (dashed line), together with the measured EL curve (dotted line, from Ref. 33). The spectral range of the FP comb at ω_2 and of the single DFB mode at ω_1 is indicated by the shaded area and dashed line, respectively. (b) Simulated level broadening γ_i (circles) and relative level occupation ρ_{ii} (squares) of the extended states (open marks) and tight-binding states (filled marks) for one QCL energy period as a function of the subband energy [see Fig. 4(a)].

approach it acts more like an electron trap. With the given average doping of the active region $\sim 2.1 \times 10^{22}$ m^{-3} (Ref. 33), we obtain mean population inversion densities $\Delta N_{5,\mathrm{ext}} \approx 1.9 \times 10^{21}$ m^{-3}, $\Delta N_{5,\mathrm{tb}} \approx 2.5 \times 10^{21}$ m^{-3}, and $\Delta N_{4,\mathrm{ext}} \approx 2.8 \times 10^{21}$ m^{-3} for extended and tight-binding states, respectively. The level broadenings of lower laser levels are almost identical for extended and tight-binding states, where we obtain the averaged values $\gamma_1 = 7.96$ meV and $\gamma_2 = 8.14$ meV. For the two upper laser levels in the tight-binding approach, the level broadenings $\gamma_4 = 11.17$ meV and $\gamma_5 = 11.66$ meV are extracted from the EMC simulations and are relatively high due to tunneling contributions. In comparison, the corresponding level broadenings for the extended states are considerably smaller, with $\gamma_4 = 6.66$ meV and $\gamma_5 = 7.02$ meV. In Fig. 4(c), the four triplets of states contributing most to the resonant second-order nonlinear susceptibility $\chi^{(2)}$ in the extended state configuration are illustrated. For the tight-binding approach, we investigate only a single triplet of states **(1)'**, which corresponds to the extended states triplet **(1)** consisting of states 5, 2, and 1. All additional parameters for the calculation of the second order nonlinear susceptibility are summarized in Table I. If we compare the pure dephasing energies for the two corresponding triplets **(1)** and **(1)'**, we identify shifts in scattering contributions. The main mechanism accounting for pure dephasing is interface roughness scattering; however, due to the extension of the upper laser levels for the actual potential V into the doping region, ionized impurity scattering plays a more important role in the extended state configuration. Taking this into account, we calculate the total dephasing energy for mid-IR transitions of triplets **(1)** and **(1)'** and obtain $\Gamma_{52,\mathrm{ext}} = 17.02$ meV, $\Gamma_{51,\mathrm{ext}} = 13.72$ meV, $\Gamma_{52,\mathrm{tb}} = 22.66$ meV, and $\Gamma_{51,\mathrm{tb}} = 18.53$ meV. These values are in good agreement with values stated in literature,[33] giving a transition linewidth of ~15–20 meV . For THz transition, total pure dephasing energies $\Gamma_{21,\mathrm{ext}} = 9.76$ meV and $\Gamma_{21,\mathrm{tb}} = 9.88$ meV are calculated, respectively. As schematically indicated in Fig. 5(a), the mid-IR pump wavelengths (λ_1, λ_2) are specified at the DFB mode $\lambda_{\mathrm{DFB}} = 7.25$ μm and at FP modes around $\lambda_{\mathrm{FP}} \sim 7.81$ μm. The transition dipole moments and calculated susceptibilities $\chi^{(2)}(\omega_{\mathrm{THz}} = \omega_{\mathrm{DFB}} - \omega_{\mathrm{FP}})$ for the five triplets are listed in Table I. The four triplets in extended state configuration add up constructively, resulting in a total susceptibility value $|\chi^{(2)}| = 7.82$ nm V^{-1}. For the tight-binding triplet **(1)'**, a total value $|\chi^{(2)}| = 6.03$ nm V^{-1} is obtained. The values are somewhat smaller than the one given in Ref. 33 of $|\chi^{(2)}| = 20$ nm V^{-1}. This is attributed to the fact that the given wavelengths λ_{DFB} and λ_{FP} could be inappropriate for the calculation of $|\chi^{(2)}|$ based on simulation results, as we obtain a blue shift (~40 cm^{-1}) compared to the experimental data.

TABLE I. Near-resonance DFG triplets of states and resulting second-order nonlinear susceptibility $\chi^{(2)}$ for the SPR-depopulation QCL active gain medium. All parameters are considered for extended states, except the triplet of state **(1)'**, where the tight-binding solutions are presented. Resonance energy $\hbar\omega_{ij}$, pure dephasing energy $\gamma_{ij,\mathrm{p}}$ (interface roughness contribution) in meV and transition dipole moments z_{ij} in nm for the mid-IR pump frequencies (ω_1, ω_2), and the THz mode (ω_{THz}).

	ω_1			ω_2			ω_{THz}		
Triplet	$\hbar\omega_{ij}$	z_{ij}	$\gamma_{ij,\mathrm{p}}$	$\hbar\omega_{ij}$	z_{ij}	$\gamma_{ij,\mathrm{p}}$	z_{ij}	$\gamma_{ij,\mathrm{p}}$	$\chi^{(2)}$/nm V^{-1}
(1)	184.7	1.15	6.18(61%)	166.6	1.01	9.55(55%)	7.99	1.76(75%)	$-1.79 + 1.42\,i$
(1)'	178.3	−1.49	8.60(80%)	160.2	1.30	12.83(72%)	8.07	1.77(75%)	$-4.99 + 3.38\,i$
(2)	166.6	1.01	9.55(55%)	153.5	−0.65	11.46(40%)	6.58	2.37(68%)	$-2.04 + 0.31\,i$
(3)	171.5	−0.75	8.28(42%)				7.99	1.76(75%)	$-1.55 + 1.25\,i$
(4)	184.7	1.15	7.57(50%)	171.5	−0.75	8.28(56%)	6.58	2.38(68%)	$-1.89 + 0.09\,i$

2. Dual-upper state active region

The investigated QCL is based on a DAU active region with $\lambda \sim 6.8\,\mu m$ and consists of strain-compensated InGaAs/InAlAs layers; experimental data can be found in Refs. 22, 34, and 90. For the operation temperature of 78 K, a CBO of 670 meV is calculated. As depicted in Fig. 4(b), the active gain medium constitutes 12 wavefunctions per period with two strongly anticrossed upper and multiple lower laser levels (miniband). Injection takes place via resonant tunneling from the electron states of the adjacent period. In the simulation, tunneling transitions from the lowest lying injector level into the upper laser levels 4, 5 are found to be the strongest with coupling strengths of $2\hbar\Omega_{56} = 8.8$ meV and $2\hbar\Omega_{54} = 8.6$ meV, respectively. Multiple lasing channels from the upper laser levels to the lower lying miniband, featuring equal transition oscillator strengths, contribute to an extremely broad gain spectrum.[90] An improved device performance at room temperature compared to the BTC designs is obtained even without the need of heterogeneous cascades. In Fig. 6(a), the simulated and normalized gain curves for operating temperatures of 78 K and 300 K are depicted. Additionally, the measured EL spectrum from Ref. 90 for a mesa device in pulsed operation at a bias of 56.9kV cm^{-1} ($V = 13.7$ V) and a temperature of 300 K is plotted. The simulated linewidth of ~ 484 cm^{-1} compares well with the experimentally measured linewidth of $\sim$490 cm^{-1}. The linewidth of DAU QCL designs is quite insensitive to bias variations due to similar spatial localization of the upper laser levels.[90] In Fig. 4(d), the five triplets of states contributing most to the resonant second-order nonlinear susceptibility $\chi^{(2)}$ are illustrated. All important microscopic quantities relevant for the determination of optical nonlinearity can be extracted from carrier transport simulations. In Fig. 6(b), the level broadening γ_i and the relative level occupation ρ_{ii} in the relevant period as a function of the subband energy are shown. For relative occupations of five levels contributing most to the optical gain and to the nonlinear mixing process, we simulate $\rho_{11} = 0.038$, $\rho_{22} = 0.036$, $\rho_{33} = 0.030$, $\rho_{44} = 0.202$, and $\rho_{66} = 0.094$. The mean population inversion density between upper laser levels 6, 4 and depleted miniband (3, 2, 1) is $\Delta N \approx 2.8 \times 10^{21}$ m^{-3} and $\Delta N \approx 1 \times 10^{21}$ m^{-3}, respectively. Furthermore, level broadenings $\gamma_1 = 5.69$ meV, $\gamma_2 = 4.58$ meV, $\gamma_3 = 4.22$ meV, and $\gamma_4 = 5.61$ meV are obtained. For the upper laser level 6, we obtain a relatively high level broadening $\gamma_6 = 11.65$ meV compared to the other levels, which is mainly due to increased interface roughness scattering from the second upper laser level 4. For carrier transport simulation of the DAU QCL design, we choose an average interface roughness height $\Delta = 0.1$ nm and a correlation length $\Lambda = 10$ nm. According to Eq. (11) and the pure dephasing rates of Table II, we calculate the total dephasing energies for five mid-IR transitions to be in the range of 12.5–16.7 meV, resulting in slightly higher values compared to the experimental estimate of 12.5 meV given in Refs. 22 and 41. In literature, the additional linewidth broadening in strain-compensated DFG-QCLs is associated with the increased CBO and pronounced interface roughness.[33,94] The contribution of interface roughness to pure dephasing energy for investigated triplets is illustrated in Table II, yielding a significant impact for mid-IR transitions. Taking also into account the reasonable match of simulated linewidth and experimental data, our simulated dephasing energies for the mid-IR regime appears to be reasonable. For the three investigated THz transitions, we obtain the total dephasing energy $\Gamma_{21} = 5.65$ meV, $\Gamma_{32} = 4.98$ meV, and $\Gamma_{64} = 9.24$ meV. The simulated THz values in the miniband compare well with the experimental assumption of 4 meV from Refs. 22 and 41, except for the increased dephasing rate Γ_{64} arising from a larger level broadening γ_6 due to interface roughness. As it is schematically indicated in Fig. 6(a), the mid-IR pump wavelengths (λ_1, λ_2) are specified at the DFB mode $\lambda_{DFB} = 6.5\,\mu m$ and at FP modes around $\lambda_{FP} \sim 6.9\,\mu m$. The transition dipole moments and calculated susceptibilities $\chi^{(2)}(\omega_{THz} = \omega_{DFB} - \omega_{FP})$ for the five triplets are listed in Table II. The five triplets contribute constructively, although the product of transition dipole moments for the triplets **(3)** and **(4)** differs from the others in sign. This stems from alternative DFG configurations of triplets illustrated schematically in Fig. 4(d). Summing up the individual contributions for the given frequency ω_{THz}, a total second-order nonlinear susceptibility value $|\chi^{(2)}| = 12.6$ nm V^{-1} is obtained, which is slightly higher than the experimental estimate of $|\chi^{(2)}| = 7.8$ nm V^{-1}.

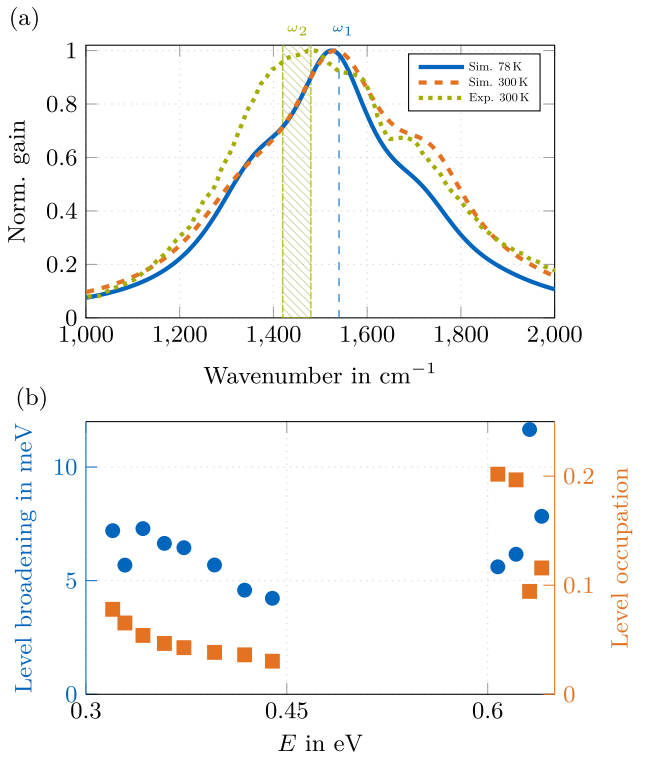

FIG. 6. Simulation results of the DAU design. (a) Normalized gain as a function of wavenumber simulated at an operating temperature of 78 K (solid line) and 300 K (dashed line) together with the measured EL curve (dotted line, from Ref. 90). Spectral range of the FP comb at ω_2 and single DFB mode at ω_1 are indicated by the shaded area and dashed line, respectively. (b) Simulated level broadening γ_i (circles) and relative level occupation ρ_{ii} (squares) for one QCL energy period as a function of the subband energy [see Fig. 4(b)].

TABLE II. Near-resonance DFG triplets of states and resulting second-order nonlinear susceptibility $\chi^{(2)}$ for the DAU QCL active gain medium. Resonance energy $\hbar\omega_{ij}$, pure dephasing energy $\gamma_{ij,\mathrm{p}}$ (interface roughness contribution) in meV and transition dipole moments z_{ij} in nm for the mid-IR pump frequencies (ω_1, ω_2), and the THz mode (ω_{THz}).

	ω_1			ω_2			ω_{THz}		
Triplet	$\hbar\omega_{ij}$	z_{ij}	$\gamma_{ij,\mathrm{p}}$	$\hbar\omega_{ij}$	z_{ij}	$\gamma_{ij,\mathrm{p}}$	z_{ij}	$\gamma_{ij,\mathrm{p}}$	$\chi^{(2)}$/nm V^{-1}
(1)	189	1.43	7.46(80%)	168.3	−1.17	9.83(68%)	−6.99	0.58(31%)	$-1.92 + 6.51\,i$
(2)	211.5	−0.54	8.98(69%)	189	1.43	7.46(80%)	−8.16	0.51(47%)	$-0.97 + 1.59\,i$
(3)	212.8	1.15	5.84(82%)				−5.05	0.61(95%)	$-1.50 + 0.84\,i$
(4)	192.1	−1.19	8.77(70%)	168.3	−1.17	9.83(68%)			$-0.24 + 1.71\,i$
(5)	212.8	1.15	6.17(61%)	192.1	−1.19	8.28(42%)	−6.99	2.37(68%)	$-0.44 + 0.90\,i$

B. DFG-QCL frequency comb simulations

In this section, we present dynamical simulation results of THz DFG-QCL frequency comb emission for the two different QCL setups. The description of the quantum mechanical system is derived from stationary carrier transport simulations. Furthermore, waveguide models for both QCL designs have to be specified and added to the simulation input script. Here, the investigated setups are based on integrated DFB gratings, defined in the experimental papers (Refs. 47 and 48). The different DFB waveguide models are compared to the common FP waveguide model, as it is illustrated in Fig. 7. For the characterization of DFB gratings, usually the coupling constant κ is used, which basically describes the field reflectance per unit length. In a first-order structure, the period length is defined by $\Lambda = \lambda_{\mathrm{B}}/2n_{\mathrm{eff}}$ with the effective refractive index n_{eff} and the Bragg wavelength λ_{B}. It is assumed that the DFB wavelength $\lambda_{\mathrm{DFB}} \approx \lambda_{\mathrm{B}}$. We could derive from test simulations that the Bragg wavelength λ_{B} should be set roughly 0.1 μm smaller than the desired DFB wavelength λ_{DFB}. The coupling constant κ of the DFB grating is defined within the coupled-mode theory and can be written as[97,98]

$$\kappa = \frac{\pi}{\lambda_{\mathrm{DFB}}}\frac{\Delta n}{2}, \tag{13}$$

where Δn is the modulation of the modal refractive index n_{eff}.

1. Single-phonon resonance depopulation structure

For the dynamical simulation of the SPR-depopulation setup, we use the carrier transport simulation results obtained for the tight-binding potential at a bias of 45kV cm^{-1}. One tunneling pair is specified and the corresponding Rabi frequency Ω_{45} is added to the Hamiltonian. Two DFG triplets comprising one upper laser level and three lower laser levels are added. By taking into account these transitions for the dipole moment operator and the pure dephasing rates, we derive the complete quantum mechanical description for the reduced SPR-depopulation structure.

Here, a 4 mm-long waveguide is patterned with a 1.5 mm DFB grating and terminated with an HR-coated back facet. The single period DFB grating defined by e-beam lithography and dry etching is designed for single mode DFB lasing at $\lambda_{\mathrm{DFB}} = 7.25\,\mu$m, which is detuned by 80 cm^{-1} from the FP comb emission frequency to minimize laser dispersion effected by the DFB structure. Due to the fact that the simulated gain curve is blue-shifted by roughly ∼40 cm^{-1} compared to the measured EL spectrum extracted from Ref. 33, we decided to choose a DFB frequency of $\lambda_{\mathrm{DFB}} = 6.8\,\mu$m to retrieve the correct THz DFG frequency comb behavior. The DFB grating is defined by a period length $\Lambda = 1.15$ μm, and a coupling constant $\kappa = 35$ cm^{-1} was estimated from the experimental subthreshold emission spectra. For our simulation, we set

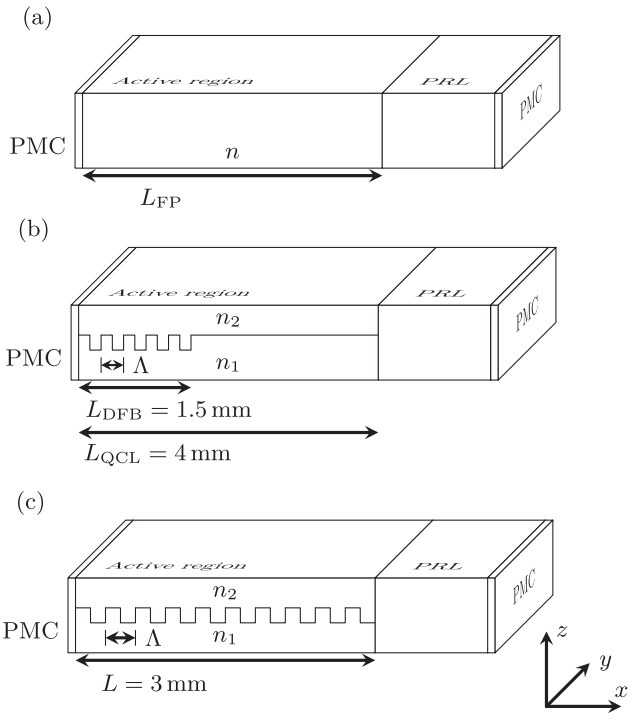

FIG. 7. Simulation setups for the Maxwell–Bloch simulation of the two considered THz DFG-QCL frequency comb setups. (a) FP reference waveguide model. (b) Waveguide model of the SPR-depopulation QCL setup including a single-period DFB grating. (c) Waveguide model of the DAU QCL design including a single-period DFB grating.

$\kappa_{sim} = 20\ cm^{-1}$, as a simulative characterization of the DFB grating indicates this as best fit for a spectral seperation of 3.5 cm^{-1} from the DFB wavenumber. Furthermore, an effective refractive index $n_{eff} = 3$ with a modulation $\Delta n = 1.5 \times 10^{-2}$ is calculated. We use $N_z = 20\,000$ spatial gridpoints and set a simulation endtime of 50 ns, corresponding to ~600 roundtrips. The resulting Python script that starts a simulation in mbsolve is depicted in Sec. II A of the supplementary material. Here, a simulation time step of 1ns takes approximately 45 min with a machine based on two AMD Epyc 7713 sockets with 64 cores each and 512 GB of RAM.

The obtained simulation results for the mid-IR spectrum and THz frequency comb of the SPR-depopulation setup are depicted in Figs. 8(a) and 8(b), respectively. Broadband FP frequency comb emission is obtained at a wavelength of around $\lambda_{FP} \sim 7.55\ \mu m$, which is slightly lower than the measured one at 7.81 μm and can be attributed to the blue shifted gain in the simulation. By mixing the mid-IR FP comb with the DFB reference mode, a THz comb extending from 3.5 to 4.5 THz is generated. In comparison to the experimental data, which are presented in Ref. 47 and where the THz DFG frequency comb is located around 3 THz, a small blueshift is obtained. A smaller sidecomb extending from 4.7 to 5.5 THz is also visible, which is more than one order of magnitude smaller as compared to the main comb. Furthermore, we investigate the amplitude and phase dynamics of the field at the facet in both mid-IR and THz regimes. A reference simulation without DFB grating shows a linearly chirped instantaneous frequency, indicating a locked FM-comb state. The results are depicted in Fig. 1 in the supplementary material.

Besides this well studied state, we analyze the temporal characteristic of the DFG-QCL setup within the DFB waveguide configuration shown in Fig. 7(b). The obtained results for the mid-IR and THz regimes are illustrated in Figs. 9(a) and 9(b), respectively. The temporal evolution of the instantaneous frequency in the mid-IR regime clearly shows linear behavior from 1 300 cm^{-1}–1 365 cm^{-1}, thus covering the whole FP frequency comb given in Fig. 8(a). Furthermore, the distinct AM state with a very short characteristic spike at the end of the periodic time signal is in good agreement with experimental and theoretical findings.[10,14] In comparison to the FP setup, we see a clear redshift of the mid-IR comb arising from mode suppression introduced by the DFB grating. In the temporal dynamics of the mid-IR component, shown in Fig. 9(a), we identify numerous very fast intensity modulations, which are

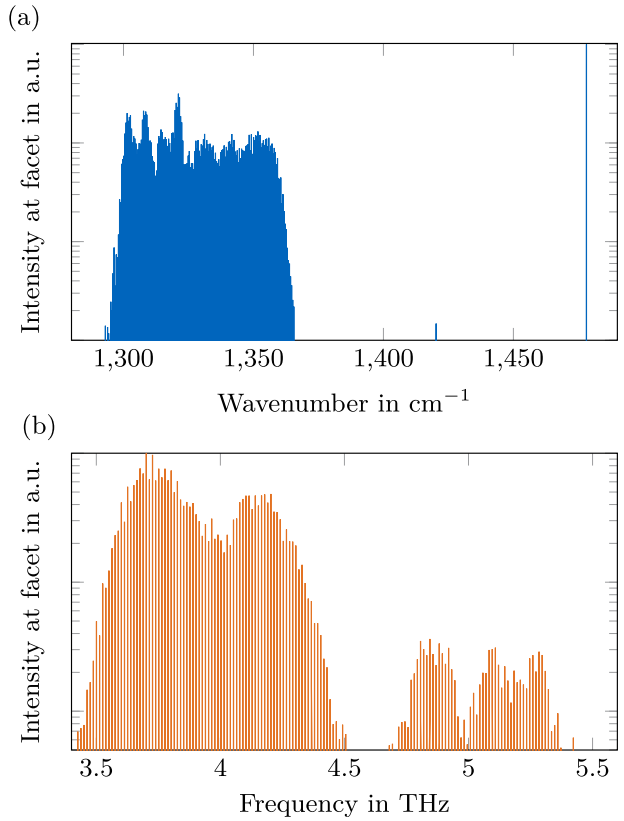

FIG. 8. Simulated mid-IR (a) and THz (b) spectra of the DFG-QCL at a temperature of 293 K and an applied bias of 45kV cm^{-1}. Experimental results are presented in Ref. 47.

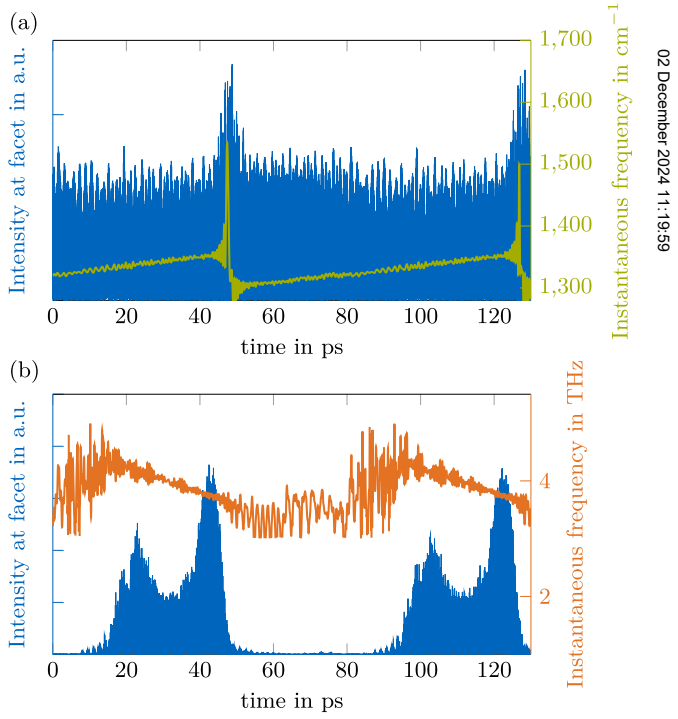

FIG. 9. Simulation results of the DFG-QCL device at a temperature of 293 K. The simulation parameters are determined in EMC simulations for a bias of 45 kV cm^{-1}. Simulated instantaneous intensity at the facet and calculated instantaneous frequency from the Hilbert transform of the simulated electric field for mid-IR FP components (a) and THz components (b).

absent in mid-IR combs without DFB grating [compare to Fig. 1(b) in the supplementary material and Ref. 6]. The reconstructed time trace of the THz signal is illustrated in Fig. 9(b). Here, a linear chirp over a considerable part of the roundtrip time is identified and extends from 3.5 to 4.5 THz, corresponding to the dominant lobe of the simulated THz spectrum in Fig. 8(b). The THz signal shows a mirrored characteristic as compared to the mid-IR signal, which illustrates coupling arising from DFG mixing.

2. Dual-upper state active region

In the carrier transport simulations, we have identified five main DFG triplets formed by different combinations of the two upper laser levels 6 and 4 and three lower laser levels 3, 2, and 1, as illustrated in Fig. 4(d). The dipole moments of all mid-IR transitions (ω_1, ω_2) and THz transitions are added to the dipole moment operator. Carrier injection is modeled by resonant tunneling, where four anticrossed tunneling pairs, formed by two injector states (7, 5) and two upper laser levels (6, 4), are included. The calculated anticrossing energies are added to the system Hamiltonian $\hat{H}_s$. For all quantum coherence terms considered in our Maxwell–Bloch model, we have to add the corresponding pure dephasing rates, while the level broadenings γ_i are directly calculated from the specified scattering rate matrix. Both terms are summarized in a relaxation superoperator class object and form together with the system Hamiltonian $\hat{H}_s$ and dipole operator $\hat{d}$, the quantum mechanical description of the active region.

The QCL waveguide consists of a single period DFB grating, which is defined by nanoimprint lithography. The first order grating period is $\Lambda = 1.04\,\mu\text{m}$. To avoid suppression of broadband FP comb emission, the DFB mode has to be largely detuned from the gain maximum. Here, the single-mode DFB wavelength is chosen to be $\lambda_{\text{DFB}} = 6.5\,\mu\text{m}$ and FP frequency comb modes are generated around $\lambda_{\text{FP}} = 6.9\,\mu\text{m}$. The coupling constant is estimated in Ref. 48 as $\kappa \sim 7\,\text{cm}^{-1}$. Based on that, we calculate an effective refractive index $n_{\text{eff}} = 3.08$ with a modulation $\Delta n = 2.9 \times 10^{-2}$ for the DFB grating. An overlap factor $\Gamma = 0.6$ and field losses $\alpha_0 = 3.2\,\text{cm}^{-1}$ are assumed for the two materials comprising the DFB grating period. The device with a cavity length $L = 3$ mm is HR coated on the back facet, and for the front facet, we use PRL boundary conditions specified by the reflectance $R = |n_{\text{eff}} - 1|^2/|n_{\text{eff}} + 1|^2$. To assure an adequate spatial discretization, we specify the number of spatial gridpoints $N_z = 15\,000$. The simulation endtime was set to 100 ns, which equals around ~ 1500 roundtrips. The simulation setup consisting of a device and a scenario is summarized in a Python script, which is depicted in Sec. II A of the supplementary material and can be used to start a dynamical DFG-QCL simulation with the open source tool mbsolve. For this quite complex and computationally demanding application, we use a machine based on two AMD Epyc 7713 sockets. Nevertheless, a simulation time of 1 ns takes approximately 45 min.

The obtained DFG-QCL simulation results are depicted in Fig. 10(a) for the mid-IR spectrum and in Fig. 10(b) for the THz frequency emission. We clearly identify a single DFB mode, which proves the validity of the implementation of the DFB grating in the mbsolve simulation framework.

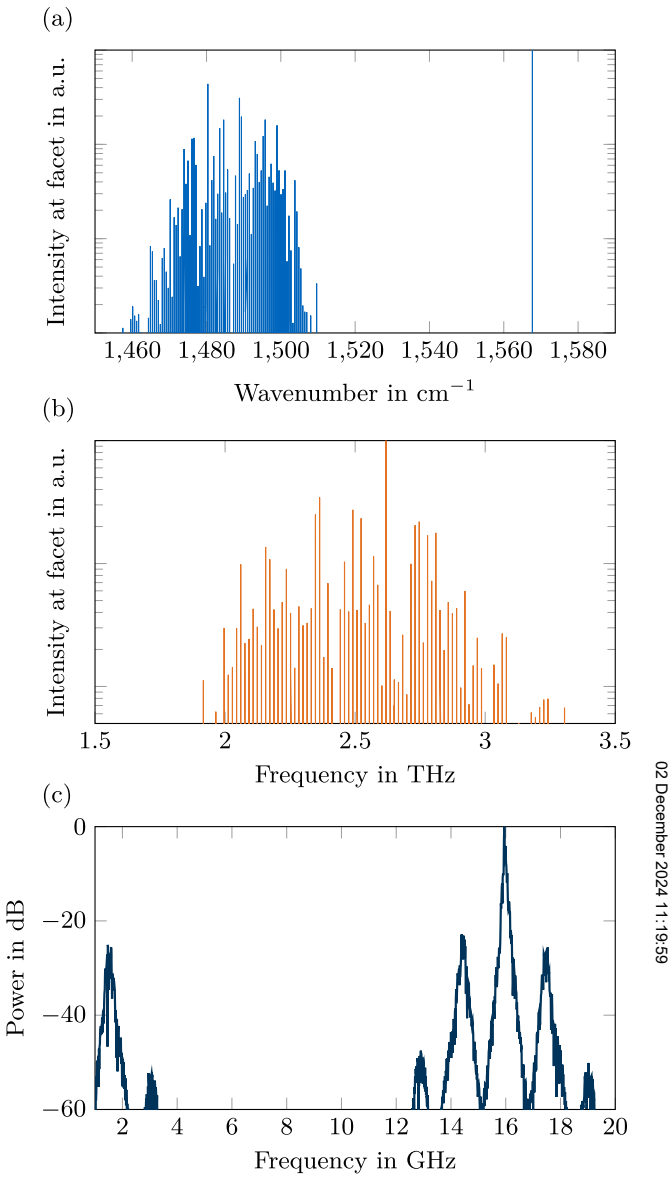

FIG. 10. Simulated mid-IR (a), THz (b) spectra, and RF beatnote (c) of the DFG-QCL at a temperature of 78 K and a bias of 56 kV cm^{-1}. Experimental results are presented in Ref. 48.

As our simulated gain curve exhibits a slight blue shift in comparison to experimental results, also the simulated mid-IR FP spectrum is slightly shifted toward higher frequencies, relative to the measured spectrum in Ref. 48. The simulated spectrum spans from $\sim$1 460 cm^{-1}–1 510 cm^{-1}, which is still in good agreement with the experimental bandwidth. To compensate for that, we decided to also shift the DFB mode in simulations toward a higher

wavenumber of 1567 cm^{-1}. The intracavity mixing between the mid-IR FP multimodes and single DFB mode results in an down-conversion toward the THz spectrum extending from 1.9 to 3.3 THz. The simulation results are in reasonable agreement with the experimentally measured ultra-broadband THz emission extending from 1.8 to 3.3 THz, as reported in Ref. 48. In the experiment, a relatively flat plateau at the gain peak was measured, which constitutes a relative gain variation of less than 5% within the FP spectral range of 1420 cm^{-1} to 1480 cm^{-1}. In contrast, a more distinct gain peak is obtained in the stationary carrier transport simulations. Here, a relative gain variation of ∼20% in the aforementioned FP spectral range is calculated. The mid-IR FP bandwidth and in consequence the THz spectrum shows a more pronounced lobe for the dynamical simulation, resulting in less intense sidemodes.

Additionally, we analyze the radio frequency (RF) beatnote of the electric field at the facet, depicted in Fig. 10(c). The main peak at 16 GHz corresponds to the inverse of the roundtrip time. Two additional beatnotes appear in the RF spectrum close to the main beatnote, at 14.5 and 17.5 GHz, as well as higher order sidebands. Therefore, a narrow beatnote spacing of 1.5 GHz is given, which can be explained by the formation of sub-combs. Similar behavior has been observed in Ref. 99, where the dynamics of comb formation in THz QCLs were investigated. The emergence of spectrally separated sub-combs was previously also detected in microresonator combs, where four-wave mixing processes induce mode proliferation.[100] The sidepeaks in the RF signal arise from the coexisting sub-combs in the cavity, which feature same mode spacing, but exhibit slightly different carrier offset frequencies. At the simulated bias point of 56 kV cm^{-1}, the DFG QCL device appears to not fully operate in the stable fundamental frequency comb regime in our simulations. It rather exhibits a state where the coexistence of different sub-combs hinders the build-up of a fundamental comb. In the time-trace of the intensity and instantaneous frequency, this results in alternating frequency and amplitude modulated behavior (see Fig. 3 in the supplementary material), similar to the results in Ref. 10. Even in this state, the emission of multimode THz radiation could be simulated and can unambiguously be assigned to the DFG process in a mid-IR QCL, necessitating the elaborate full-wave approach. In order to retrieve a complete understanding of different dynamical regimes, including the fully locked DFG QCL comb state, a detailed study with an extended bias sweep would be required and will be addressed in future works.

IV. CONCLUSION

In this paper, we have presented THz DFG-QCL frequency comb simulation results based on a self-consistent multi-domain simulation approach, which couples an open-source Maxwell-Bloch solver to a stationary carrier transport simulation approach based on the Monte Carlo method. For the calculation of important material parameters, e.g., CBO, we fully take into account important environmental influences such as strain and nonparabolicity effects. We have investigated the THz frequency comb formation by DFG in two QCL designs, consisting of a single-phonon resonance depopulation scheme and a dual-upper state active region, respectively. The experimentally obtained broad gain curve and calculated high second-order nonlinearity are closely reproduced by our stationary carrier transport simulations. Furthermore, we have performed dynamical full-wave simulations of THz frequency comb emission based on difference frequency generation for both setups, where the THz comb is obtained by nonlinear mixing of a largely detuned DFB mid-IR single mode and a mid-IR FP comb. All in all, the THz DFG-QCL comb results are in good agreement with experimental measurements. For the SPR-depopulation QCL setup, we obtain a linear instantaneous frequency chirp at the investigated bias, in reasonable agreement with experimental findings. Furthermore, the obtained THz time-trace follows the mid-IR signal and, thus, corroborates the concept of DFB downconversion from the mid-IR FP comb into a THz comb. In the dynamical simulations of the dual-upper state DFG QCL setup at the investigated bias, we identify sidepeaks in the RF beatnote spectrum, indicating the coexistence of sub-combs, which affect the modulation behavior of the fundamental comb. For both setups, the simulated mid-IR FP frequency comb is slightly shifted toward higher frequencies. Therefore, we obtain a smaller frequency gap between FP comb and DFB mode with respect to the experimental data, and the resulting THz frequency comb is somewhat red-shifted. We obtain broad THz spectra for both designs and reproduce the measured ultra-broadband THz emission in the DAU device. The reasonable agreement with experimental data shows that our simulation approach contains all relevant effects. Thus, it constitutes a suitable tool for systematic design optimization of THz DFG-QCL comb structures, which may be accelerated by using a lower level quantum system model featuring all optical and nonlinear effects responsible for the DFG description.

SUPPLEMENTARY MATERIAL

See the supplementary material for additional temporal and spectral results that may be helpful for the correct interpretation of the results. Additionally, the Python scripts to set up and run mbsolve simulations of both THz DFG-QCL setups are provided in the supplementary material.

ACKNOWLEDGMENTS

The authors acknowledge financial support by the European Union's QuantERA II (G.A. No. 101 017 733)—QATACOMB Project "Quantum correlations in terahertz QCL combs" [Funding organisations: DFG—Germany (Project No. 491 801 597), CNR—Italy]; by the European Union's NextGenerationEU Programme with the I-PHOQS Infrastructure (Nos. IR0000016, ID D2B8D520, and CUP B53C22001750006) "Integrated infrastructure initiative in Photonic and Quantum Sciences"; by the European Union's Research and Innovation Programmes Horizon 2020 and Horizon Europe with the Qombs Project (G.A. No. 820 419) "Quantum simulation and entanglement engineering in quantum cascade laser frequency combs," the Laserlab-Europe Project (G.A. No. 871 124), and the MUQUABIS Project (G.A. No. 101 070 546) "Multiscale quantum bio-imaging and spectroscopy;" and by the Italian ESFRI Roadmap (Extreme Light Infrastructure—ELI Project).

AUTHOR DECLARATIONS

Conflict of Interest

The authors have no conflicts to disclose.

Author Contributions

Johannes Popp: Conceptualization (lead); Data curation (equal); Formal analysis (equal); Investigation (lead); Methodology (lead); Software (equal); Validation (equal); Visualization (lead); Writing – original draft (lead); Writing – review & editing (lead). **Lukas Seitner:** Conceptualization (supporting); Software (equal); Validation (equal); Visualization (equal); Writing – original draft (supporting); Writing – review & editing (equal). **Michael A. Schreiber:** Conceptualization (supporting); Software (equal); Validation (supporting); Visualization (supporting); Writing – original draft (supporting); Writing – review & editing (supporting). **Michael Haider:** Conceptualization (supporting); Data curation (equal); Funding acquisition (supporting); Investigation (supporting); Project administration (supporting); Software (equal); Supervision (supporting); Validation (equal); Visualization (supporting); Writing – original draft (supporting); Writing – review & editing (equal). **Luigi Consolino:** Conceptualization (supporting); Funding acquisition (supporting); Investigation (supporting); Methodology (supporting); Project administration (equal); Validation (equal); Visualization (supporting); Writing – original draft (supporting); Writing – review & editing (supporting). **Alessia Sorgi:** Conceptualization (supporting); Investigation (supporting); Methodology (supporting); Validation (supporting); Visualization (supporting); Writing – original draft (supporting); Writing – review & editing (supporting). **Francesco Cappelli:** Conceptualization (supporting); Funding acquisition (supporting); Investigation (supporting); Methodology (supporting); Validation (supporting); Visualization (supporting); Writing – original draft (supporting); Writing – review & editing (supporting). **Paolo De Natale:** Conceptualization (supporting); Funding acquisition (supporting); Investigation (supporting); Methodology (supporting); Supervision (supporting); Validation (supporting); Visualization (supporting); Writing – original draft (supporting); Writing – review & editing (supporting). **Kazuue Fujita:** Conceptualization (supporting); Investigation (supporting); Methodology (supporting); Validation (equal); Visualization (supporting); Writing – original draft (supporting); Writing – review & editing (supporting). **Christian Jirauschek:** Conceptualization (supporting); Data curation (supporting); Formal analysis (supporting); Funding acquisition (lead); Investigation (equal); Methodology (equal); Project administration (equal); Resources (lead); Software (equal); Supervision (lead); Validation (equal); Visualization (supporting); Writing – original draft (supporting); Writing – review & editing (equal).

DATA AVAILABILITY

The data that support the findings of this study are available from the corresponding author upon reasonable request.

REFERENCES

[1]D. Burghoff, T.-Y. Kao, N. Han, C. W. I. Chan, X. Cai, Y. Yang, D. J. Hayton, J.-R. Gao, J. L. Reno, and Q. Hu, Nat. Photonics **8**, 462 (2014).
[2]A. Hugi, G. Villares, S. Blaser, H. C. Liu, and J. Faist, Nature **492**, 229 (2012).
[3]K. Garrasi, F. P. Mezzapesa, L. Salemi, L. Li, L. Consolino, S. Bartalini, P. De Natale, A. G. Davies, E. H. Linfield, and M. S. Vitiello, ACS Photonics **6**, 73 (2019).
[4]M. Rösch, G. Scalari, M. Beck, and J. Faist, Nat. Photonics **9**, 42 (2015).
[5]M. Rösch, M. Beck, M. J. Süess, D. Bachmann, K. Unterrainer, J. Faist, and G. Scalari, Nanophotonics **7**, 237 (2018).
[6]E. Riccardi, V. Pistore, L. Consolino, A. Sorgi, F. Cappelli, R. Eramo, P. De Natale, L. Li, A. G. Davies, E. H. Linfield, and M. S. Vitiello, Laser Photonics Rev. **17**, 2200412 (2023).
[7]L. Consolino, M. Nafa, F. Cappelli, K. Garrasi, F. P. Mezzapesa, L. Li, A. G. Davies, E. H. Linfield, M. S. Vitiello, P. De Natale, and S. Bartalini, Nat. Commun. **10**, 2938 (2019).
[8]T. Udem, R. Holzwarth, and T. W. Hänsch, Nature **416**, 233 (2002).
[9]D. Burghoff, Y. Yang, D. J. Hayton, J.-R. Gao, J. L. Reno, and Q. Hu, Opt. Express **23**, 1190 (2015).
[10]M. Singleton, P. Jouy, M. Beck, and J. Faist, Optica **5**, 948 (2018).
[11]F. Cappelli, L. Consolino, G. Campo, I. Galli, D. Mazzotti, A. Campa, M. Siciliani de Cumis, P. Cancio Pastor, R. Eramo, M. Rösch, M. Beck, G. Scalari, J. Faist, P. De Natale, and S. Bartalini, Nat. Photonics **13**, 562 (2019).
[12]E. Riccardi, V. Pistore, S. Kang, L. Seitner, A. De Vetter, C. Jirauschek, J. Mangeney, L. Li, A. G. Davies, E. H. Linfield, A. C. Ferrari, S. S. Dhillon, and M. S. Vitiello, Nat. Photonics **17**, 1 (2023).
[13]J. Hillbrand, A. M. Andrews, H. Detz, G. Strasser, and B. Schwarz, Nat. Photonics **13**, 101 (2019).
[14]J. B. Khurgin, Y. Dikmelik, A. Hugi, and J. Faist, Appl. Phys. Lett. **104**, 081118 (2014).
[15]C. Silvestri, L. L. Columbo, M. Brambilla, and M. Gioannini, Opt. Express **28**, 23846 (2020).
[16]C. Silvestri, X. Qi, T. Taimre, and A. D. Rakić, Phys. Rev. A **106**, 053526 (2022).
[17]N. Opačak and B. Schwarz, Phys. Rev. Lett. **123**, 243902 (2019).
[18]D. Burghoff, Optica **7**, 1781 (2020).
[19]L. Humbard and D. Burghoff, Opt. Express **30**, 5376 (2022).
[20]C. Sirtori, Nat. Photonics **15**, 1 (2021).
[21]M. A. Belkin, F. Capasso, F. Xie, A. Belyanin, M. Fischer, A. Wittmann, and J. Faist, Appl. Phys. Lett. **92**, 201101 (2008).
[22]K. Fujita, S. Jung, Y. Jiang, J. H. Kim, A. Nakanishi, A. Ito, M. Hitaka, T. Edamura, and M. A. Belkin, Nanophotonics **7**, 1795 (2018).
[23]L. Bosco, M. Franckié, G. Scalari, M. Beck, A. Wacker, and J. Faist, Appl. Phys. Lett. **115**, 010601 (2019).
[24]A. Khalatpour, A. K. Paulsen, C. Deimert, Z. R. Wasilewski, and Q. Hu, Nat. Photonics **15**, 16 (2021).
[25]M. Wienold, B. Röben, L. Schrottke, R. Sharma, A. Tahraoui, K. Biermann, and H. Grahn, Opt. Express **22**, 3334 (2014).
[26]C. A. Curwen, S. J. Addamane, J. L. Reno, M. Shahili, J. H. Kawamura, R. M. Briggs, B. S. Karasik, and B. S. Williams, AIP Adv. **11**, 125018 (2021).
[27]M. A. Belkin, F. Capasso, A. Belyanin, D. L. Sivco, A. Y. Cho, D. C. Oakley, C. J. Vineis, and G. W. Turner, Nat. Photonics **1**, 288 (2007).
[28]M. A. Belkin and F. Capasso, Phys. Scr. **90**, 118002 (2015).
[29]M. Razeghi, Q. Lu, N. Bandyopadhyay, W. Zhou, D. Heydari, Y. Bai, and S. Slivken, Opt. Express **23**, 8462 (2015).
[30]Q. Lu and M. Razeghi, Photonics **3**, 42 (2016).
[31]K. Fujita, M. Hitaka, A. Ito, T. Edamura, M. Yamanishi, S. Jung, and M. A. Belkin, Appl. Phys. Lett. **106**, 251104 (2015).
[32]K. Fujita, M. Hitaka, A. Ito, M. Yamanishi, T. Dougakiuchi, and T. Edamura, Opt. Express **24**, 16357 (2016).
[33]Q. Lu, D. Wu, S. Sengupta, S. Slivken, and M. Razeghi, Sci. Rep. **6**, 23595 (2016).

[34]K. Fujita, A. Ito, M. Hitaka, T. Dougakiuchi, and T. Edamura, Appl. Phys. Express **10**, 082102 (2017).
[35]Q. Lu, N. Bandyopadhyay, S. Slivken, Y. Bai, and M. Razeghi, Appl. Phys. Lett. **99**, 131106 (2011).
[36]K. Vijayraghavan, R. W. Adams, A. Vizbaras, M. Jang, C. Grasse, G. Boehm, M. C. Amann, and M. A. Belkin, Appl. Phys. Lett. **100**, 251104 (2012).
[37]Q. Lu, N. Bandyopadhyay, S. Slivken, Y. Bai, and M. Razeghi, Appl. Phys. Lett. **104**, 221105 (2014).
[38]A. Jiang, S. Jung, Y. Jiang, K. Vijayraghavan, J. H. Kim, and M. A. Belkin, Appl. Phys. Lett. **106**, 261107 (2015).
[39]Q. Lu, S. Slivken, N. Bandyopadhyay, Y. Bai, and M. Razeghi, Appl. Phys. Lett. **105**, 201102 (2014).
[40]S. Jung, A. Jiang, Y. Jiang, K. Vijayraghavan, X. Wang, M. Troccoli, and M. A. Belkin, Nat. Commun. **5**, 4267 (2014).
[41]K. Vijayraghavan, Y. Jiang, M. Jang, A. Jiang, K. Choutagunta, A. Vizbaras, F. Demmerle, G. Boehm, M. C. Amann, and M. A. Belkin, Nat. Commun. **4**, 2021 (2013).
[42]Y. Jiang, K. Vijayraghavan, S. Jung, F. Demmerle, G. Boehm, M. C. Amann, and M. A. Belkin, J. Opt. **16**, 094002 (2014).
[43]Y. Jiang, K. Vijayraghavan, S. Jung, A. Jiang, J. H. Kim, F. Demmerle, G. Boehm, M. C. Amann, and M. A. Belkin, Sci. Rep. **6**, 21169 (2016).
[44]L. Consolino, S. Jung, A. Campa, M. De Regis, S. Pal, J. H. Kim, K. Fujita, A. Ito, M. Hitaka, S. Bartalini, P. De Natale, M. A. Belkin, and M. Serena Vitiello, Sci. Adv. **3**, e1603317 (2017).
[45]L. Consolino, F. Cappelli, M. S. de Cumis, and P. De Natale, Nanophotonics **8**, 181 (2019).
[46]K. Fujita, S. Hayashi, A. Ito, M. Hitaka, and T. Dougakiuchi, Nanophotonics **8**, 2235 (2019).
[47]Q. Lu, F. Wang, D. Wu, S. Slivken, and M. Razeghi, Nat. Commun. **10**, 2403 (2019).
[48]L. Consolino, M. Nafa, M. De Regis, F. Cappelli, S. Bartalini, A. Ito, M. Hitaka, T. Dougakiuchi, T. Edamura, P. De Natale, and K. Fujita, Appl. Sci. **11**, 1416 (2021).
[49]R. W. Boyd, *Nonlinear Optics*, 4th ed. (Academic Press, 2020).
[50]C. Jirauschek, M. Riesch, and P. Tzenov, Adv. Theory Simul. **2**, 1900018 (2019).
[51]G. Slavcheva, J. M. Arnold, I. Wallace, and R. W. Ziolkowski, Phys. Rev. A **66**, 063418 (2002).
[52]W. Cartar, J. Mørk, and S. Hughes, Phys. Rev. A **96**, 023859 (2017).
[53]O. Hess and T. Kuhn, Phys. Rev. A **54**, 3347 (1996).
[54]C. R. Menyuk and M. A. Talukder, Phys. Rev. Lett. **102**, 023903 (2009).
[55]Y. Wang and A. Belyanin, Opt. Express **23**, 4173 (2015).
[56]L. L. Columbo, S. Barbieri, C. Sirtori, and M. Brambilla, Opt. Express **26**, 2829 (2018).
[57]P. Tzenov, I. Babushkin, R. Arkhipov, M. Arkhipov, N. Rosanov, U. Morgner, and C. Jirauschek, New J. Phys. **20**, 053055 (2018).
[58]F. Wang, V. Pistore, M. Riesch, H. Nong, P.-B. Vigneron, R. Colombelli, O. Parillaud, J. Mangeney, J. Tignon, C. Jirauschek, and S. S. Dhillon, Light Sci. Appl. **9**, 51 (2020).
[59]C. Y. Wang, L. Diehl, A. Gordon, C. Jirauschek, F. X. Kärtner, A. Belyanin, D. Bour, S. Corzine, G. Höfler, M. Troccoli, J. Faist, and F. Capasso, Phys. Rev. A **75**, 031802 (2007).
[60]A. Gordon, C. Y. Wang, L. Diehl, F. X. Kärtner, A. Belyanin, D. Bour, S. Corzine, G. Höfler, H. C. Liu, H. Schneider, T. Maier, M. Troccoli, J. Faist, and F. Capasso, Phys. Rev. A **77**, 053804 (2008).
[61]N. N. Vuković, J. Radovanović, V. Milanović, and D. L. Boiko, IEEE J. Sel. Top. Quantum Electron. **23**, 1 (2017).
[62]P. Tzenov, D. Burghoff, Q. Hu, and C. Jirauschek, Opt. Express **24**, 23232 (2016).
[63]C. Jirauschek and P. Tzenov, Opt. Quant. Electron. **49**, 414 (2017).
[64]P. Tzenov, D. Burghoff, Q. Hu, and C. Jirauschek, IEEE Trans. Terahertz Sci. Technol. **7**, 351 (2017).
[65]M. Riesch and C. Jirauschek, Comput. Phys. Commun. **268**, 108097 (2021).
[66]A. Forrer, Y. Wang, M. Beck, A. Belyanin, J. Faist, and G. Scalari, Appl. Phys. Lett. **118**, 131112 (2021).
[67]M. Piccardo, B. Schwarz, D. Kazakov, M. Beiser, N. Opačak, Y. Wang, S. Jha, J. Hillbrand, M. Tamagnone, W. T. Chen, A. Y. Zhu, L. L. Columbo, A. Belyanin, and F. Capasso, Nature **582**, 360 (2020).
[68]Y. Wang and A. Belyanin, Phys. Rev. A **102**, 013519 (2020).
[69]C. Silvestri, X. Qi, T. Taimre, K. Bertling, and A. D. Rakić, APL Photonics **8**, 020902 (2023).
[70]L. Seitner, J. Popp, M. Riesch, M. Haider, and C. Jirauschek, J. Phys.: Conf. Ser. **2090**, 012082 (2021).
[71]F. P. Mezzapesa, K. Garrasi, J. Schmidt, L. Salemi, V. Pistore, L. Li, A. G. Davies, E. H. Linfield, M. Riesch, C. Jirauschek, T. Carey, F. Torrisi, A. C. Ferrari, and M. S. Vitiello, ACS Photonics **7**, 3489 (2020).
[72]J. Popp, L. Seitner, M. Haider, and C. Jirauschek, in *2022 3rd URSI Atlantic and Asia Pacific Radio Science Meeting (AT-AP-RASC)* (IEEE, 2022), pp. 1–4.
[73]C. Jirauschek and T. Kubis, Appl. Phys. Rev. **1**, 011307 (2014).
[74]C. Jirauschek, J. Appl. Phys. **122**, 133105 (2017).
[75]M. Riesch and C. Jirauschek, see https://github.com/mriesch-tum/mbsolve for"mbsolve: An open-source solver tool for the Maxwell-Bloch equations" (2021).
[76]J. Popp, M. Haider, M. Franckié, J. Faist, and C. Jirauschek, Opt. Quant. Electron. **53**, 287 (2021).
[77]C. Jirauschek, J. Popp, M. Haider, M. Franckié, and J. Faist, J. Appl. Phys. **130**, 203103 (2021).
[78]C. G. Van de Walle, Phys. Rev. B **39**, 1871 (1989).
[79]I. Vurgaftman, J. R. Meyer, and L. R. Ram-Mohan, J. Appl. Phys. **89**, 5815 (2001).
[80]M. Sugawara, N. Okazaki, T. Fujii, and S. Yamazaki, Phys. Rev. B **48**, 8102 (1993).
[81]U. Ekenberg, Phys. Rev. B **40**, 7714 (1989).
[82]C. Jirauschek, IEEE J. Quantum Electron. **45**, 1059 (2009).
[83]V. Rindert, E. Önder, and A. Wacker, Phys. Rev. Appl. **18**, L041001 (2022).
[84]A. Taflove and S. C. Hagness, *Computational Electrodynamics: The Finite-Difference Time-Domain Method*, 3rd ed. (Artech House, Boston, 2005).
[85]J.-P. Berenger, J. Comp. Phys. **114**, 185 (1994).
[86]J. Fang and Z. Wu, IEEE Microwave Guided Wave Lett. **5**, 451 (1995).
[87]S. D. Gedney, Electromagnetics **16**, 399 (1996).
[88]S. D. Gedney, IEEE Trans. Antennas Propag. **44**, 1630 (1996).
[89]M. A. Schreiber, J. Popp, L. Seitner, M. Haider, and C. Jirauschek, in *2022 International Conference on Numerical Simulation of Optoelectronic Devices (NUSOD)* (IEEE, 2022), pp. 99–100.
[90]K. Fujita, S. Furuta, A. Sugiyama, T. Ochiai, A. Ito, T. Dougakiuchi, T. Edamura, and M. Yamanishi, Appl. Phys. Lett. **98**, 231102 (2011).
[91]C. Jirauschek, H. Okeil, and P. Lugli, Opt. Express **23**, 1670 (2015).
[92]C. Jirauschek, A. Matyas, P. Lugli, and M.-C. Amann, Opt. Express **21**, 6180 (2013).
[93]A. Mátyás, P. Lugli, and C. Jirauschek, J. Appl. Phys. **110**, 013108 (2011).
[94]S. Tsujino, A. Borak, E. Müller, M. Scheinert, C. Falub, H. Sigg, D. Grützmacher, M. Giovannini, and J. Faist, Appl. Phys. Lett. **86**, 062113 (2005).
[95]A. Wittmann, Y. Bonetti, J. Faist, E. Gini, and M. Giovannini, Appl. Phys. Lett. **93**, 141103 (2008).
[96]K. Fujita, S. Furuta, A. Sugiyama, T. Ochiai, T. Edamura, N. Akikusa, M. Yamanishi, and H. Kan, IEEE J. Quantum Electron. **46**, 683 (2010).
[97]C. Gmachl, F. Capasso, J. Faist, A. L. Hutchinson, A. Tredicucci, D. L. Sivco, J. N. Baillargeon, S. G. Chu, and A. Y. Cho, Appl. Phys. Lett. **72**, 1430 (1998).
[98]H. Kogelnik and C. Shank, J. Appl. Phys. **43**, 2327 (1972).
[99]H. Li, P. Laffaille, D. Gacemi, M. Apfel, C. Sirtori, J. Leonardon, G. Santarelli, M. Rösch, G. Scalari, M. Beck, J. Faist, W. Hänsel, R. Holzwarth, and S. Barbieri, Opt. Express **23**, 33270 (2015).
[100]T. Herr, K. Hartinger, J. Riemensberger, C. Wang, E. Gavartin, R. Holzwarth, M. Gorodetsky, and T. Kippenberg, Nat. Photonics **6**, 480 (2012).